POLITECNICO DI TORINO
Repository ISTITUZIONALE

Built-up index and fractal dimension clustering of multispectral satellite urban images

*Original*
Built-up index and fractal dimension clustering of multispectral satellite urban images / Delgadillo-Jimenez, A., Toxqui-Quitl, C., Aguilar-Vallejo, A., Padilla-Vivanco, A., Carbone, A.. - In: INTERNATIONAL JOURNAL OF DIGITAL EARTH. - ISSN 1753-8947. - 19:2(2026), pp. 1-34. [10.1080/17538947.2026.2712686]

*Availability:*
This version is available at: 11583/3015107 since: 2026-09-02T15:48:16Z

*Publisher:*
Taylor and Francis

*Published*
DOI:10.1080/17538947.2026.2712686

*Terms of use:*

This article is made available under terms and conditions as specified in the corresponding bibliographic description in the repository

*Publisher copyright*

(Article begins on next page)

17 October 2026

International Journal of Digital Earth

ISSN: 1753-8947 (Print) 1753-8955 (Online) Journal homepage: www.tandfonline.com/journals/tjde20

# Built-up index and fractal dimension clustering of multispectral satellite urban images

Armando Delgadillo-Jimenez , Carina Toxqui-Quitl , Aldo Aguilar-Vallejo , Alfonso Padilla-Vivanco & Anna Carbone

**To cite this article:** Armando Delgadillo-Jimenez , Carina Toxqui-Quitl , Aldo Aguilar-Vallejo , Alfonso Padilla-Vivanco & Anna Carbone (2026) Built-up index and fractal dimension clustering of multispectral satellite urban images, International Journal of Digital Earth, 19:2, 2712686, DOI: 10.1080/17538947.2026.2712686

**To link to this article:** https://doi.org/10.1080/17538947.2026.2712686

© 2026 The Author(s). Published by Informa UK Limited, trading as Taylor & Francis Group.

View supplementary material

Published online: 13 Aug 2026.

Submit your article to this journal

Article views: 3

View related articles

View Crossmark data

Full Terms & Conditions of access and use can be found at
https://www.tandfonline.com/action/journalInformation?journalCode=tjde20

INTERNATIONAL JOURNAL OF DIGITAL EARTH
2026, VOL. 19, NO. 2, 2712686
https://doi.org/10.1080/17538947.2026.2712686

RESEARCH ARTICLE

OPEN ACCESS Check for updates

# Built-up index and fractal dimension clustering of multispectral satellite urban images

Armando Delgadillo-Jimenez[a], Carina Toxqui-Quitl[a], Aldo Aguilar-Vallejo[a], Alfonso Padilla-Vivanco[a] and Anna Carbone[b]

[a]Computer Vision Laboratory, Universidad Politécnica de Tulancingo, Ingeniería, Hidalgo, Mexico; [b]Department of Applied Science and Technology (DISAT), Politecnico di Torino, Corso Duca degli Abruzzi, Torino, Italy

**ABSTRACT**

The urbanization variability of several European cities is quantified in terms of fractal dimension $D_f$ and built-up density $\mathcal{B}$ by using the WorldView (WV-2 European Cities and WV-ESA archive) multispectral satellite imagery collections at different spatial resolutions. The robustness and accuracy of the proposed approach are further assessed by analyzing Sentinel-2 L2A (S-2) data. The fractal dimension $D_f$ is estimated by implementing the Detrending Moving Average Algorithm (DMA). The built-up density $\mathcal{B}$ is estimated by using the Masked Built-up Extraction Index (MBEI). The analysis yields values of $D_f$ and $\mathcal{B}$ in the ranges $1.7 \div 1.9$ and $0.01 \div 0.67$, respectively, for dispersed and highly urbanized areas. The minimum volume ellipsoids (MVE) criterion is adopted to cluster the values of fractal dimension $D_f$ and built-up index $\mathcal{B}$ and classify different urbanization areas.

**ARTICLE HISTORY**
Received 9 February 2026
Accepted 28 July 2026

**KEYWORDS**
Fractal dimension; built-up density index; urban clustering; minimum volume ellipsoids; multispectral satellite imagery

## 1. Introduction

City growth positively impacts economies of scale while also bringing together undesired environmental and social degradation (Anestis and Stathakis 2024), thus requiring that the challenges posed by urban planning to be tackled from multiple perspectives (Artmann, Inostroza, and Fan 2019; Moreno-Monroy, Schiavina, and Veneri 2021). Simple statistics yielding cumulative measures (e.g. number of residents, length of roads) are unable to fully grasp the complexity of urban phenomena. Hence, multidimensional indicators are increasingly required to monitor, quantify city development, and provide public services accordingly (Huang, Liu, and Sun 2024; Sharma and Ghuge 2025; Verma and Raghubanshi 2018). The availability of high-dimensional data (Esch and Asamer, 2020) makes accurate estimates increasingly accessible in the context of unsupervised learning (Wang and Biljecki 2022), classification (Yu, Sützl, and van Reeuwijk 2023), and clustering (Suetzl, Strebel, and Rubin 2024). Robust theories and quantitative analysis provide valuable perspectives by modeling phenomena relevant to urban development. Statistical physics and complexity science offer concepts and tools with the ability to describe the emergence of collective behavior from heterogeneous data (Hendrick, Rinaldo, and Manoli 2025; Reia, Rao, and Barthelemy 2022; West 2018).

Complex urban forms can be featured in terms of probability density distributions of built-up patterns (Arvidsson, Lovsjö, and Keuschnigg 2023; Dong, Huang, and Zhang 2020; Ribeiro and Rybski 2023). Morphology and function of cities can be quantified in terms of fractal dimension $D_f$ with respect to the urban concentration at multiple scales (Batty and Longley 1987; Frankhauser 1998). Empirical and theoretical relationships between population density, built-up patterns, and fractality in periurban contexts have been discussed for a considerable number of cities in (Thomas, Frankhauser, and Frenay 2010). The fractal dimension is proposed as an indicator of environmental vulnerability in (Wu, Huang, and Guo 2025). Urban fractal dimensions have been estimated by implementing the Detrending Moving Average (DMA) algorithm on WorldView-2 images of urban area sections

**CONTACT** Anna Carbone anna.carbone@polito.it Department of Applied Science and Technology (DISAT), Politecnico di Torino, Corso Duca degli Abruzzi, 24, Torino, 10129, Italy

Supplemental data for this article can be accessed online at https://doi.org/10.1080/17538947.2026.2712686.

© 2026 The Author(s). Published by Informa UK Limited, trading as Taylor & Francis Group.
This is an Open Access article distributed under the terms of the Creative Commons Attribution License (http://creativecommons.org/licenses/by/4.0/), which permits unrestricted use, distribution, and reproduction in any medium, provided the original work is properly cited. The terms on which this article has been published allow the posting of the Accepted Manuscript in a repository by the author(s) or with their consent.

(Carbone, Luiz da Silva, and Kaniadakis 2024; Carbone, Murialdo, and Pieroni 2022). WorldView high-spatial resolution imagery lends good accuracy for land surface classification in urban environments, thus accounting for a variety of components such as buildings, roads, vegetation, soil, and water, allowing the identification of possible dependencies between spatial scales and urbanized areas (Di Martino, Iodice, and Riccio 2017). Overall, these works provide solid foundations for understanding urban patterns in terms of fractal concepts and approaches, offering valuable insights into the spatial complexity of city infrastructural and socio-economic features. Population and built-up density highlight the relevance of urban extension in the analysis of WorldView-2 (WV-2) satellite images (Jiao 2015). Spectral indices are widely employed in remote sensing to identify land surface features and monitor the environment. Constructed as mathematical combinations of reflectance values at different wavelength bands, these indices enhance the contrast between spectral responses, simplifying complex multispectral data to effectively distinguish between rural and built-up areas (Belgiu, Drăguţ, and Strobl 2014; Fenta, Yasuda, and Haregeweyn 2017; Sameen and Pradhan 2016; Waqar, Mirza, and Mumtaz 2012).

In this work, built-up index (a density quantifier) and fractal dimension (a morphology quantifier) are estimated using low and high-resolution remote sensing imagery of urban and sub-urban areas of 28 European cities (Figure 1a,b). Then, the built-up index and fractal dimension are clustered to the aim of classifying urban and sub-urban sectors over multiple spatial scales. The analyzed cities have been established and fully developed for several centuries, so their features have not changed much over the last few decades. Hence, the obtained clusters can be easily used as a standard reference for different sectors within the same cities, among different cities, or eventually against other socio-demographic cluster features. To ensure robustness and accuracy of our approach, additional data outside Europe has been analyzed.

Traditional spectral indices often struggle to distinguish between built-up areas and bare soil because of spectral similarities. Many existing methods rely on ancillary data (such as census data, OpenStreetMap layers, or multi-sensor fusion), which may not be available or regularly updated in all regions. To address

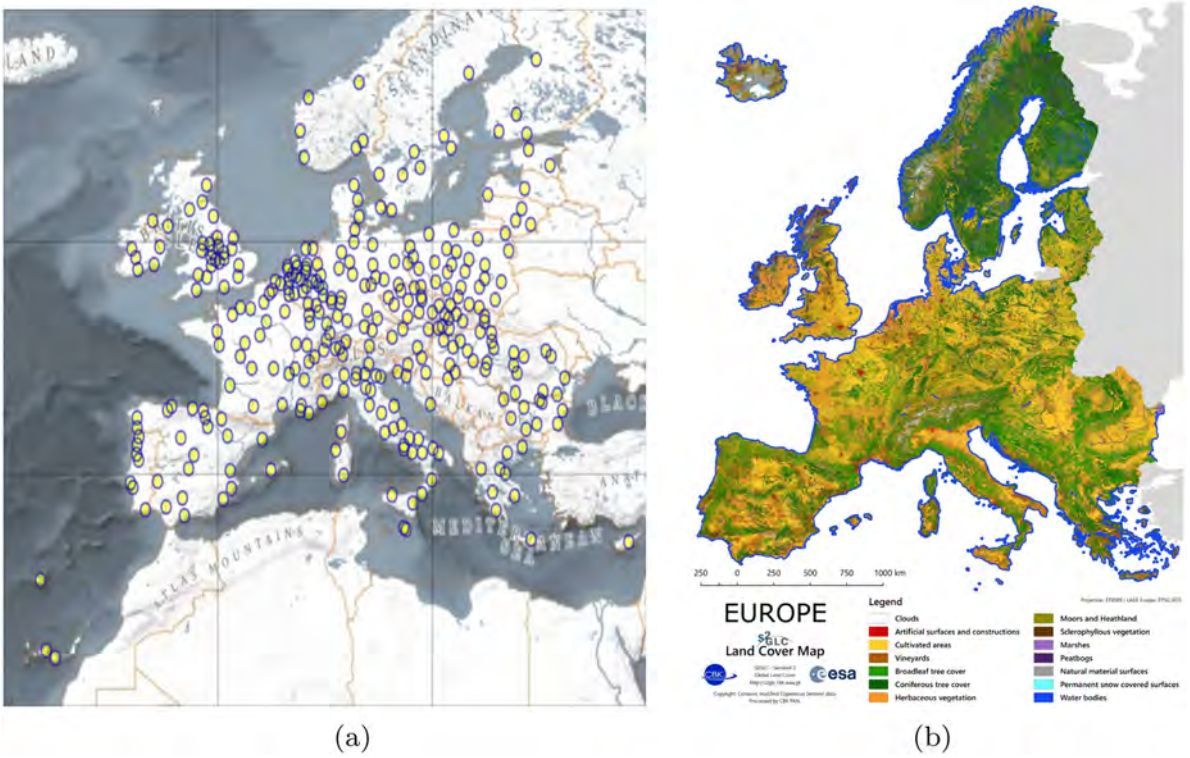


**Figure 1.** (a) WorldView-2 European Cities https://tpm-ds.eo.esa.int/smcat/WorldView-2/ (CTTO European Space Agency). (b) Europe land-cover mapped in 10 m resolution by the two identical Copernicus Sentinel-2 satellites, orbiting almost 800 km above Earth, carrying a multispectral imager able to characterize natural and artificial covers (CTTO European Space Agency).

these gaps, our proposed approach aims to be a self-contained framework. A key strength of our work is that both morphological metric ($D_f$) and physical density ($\mathcal{B}$) features are derived exclusively from the same multispectral image, without the need for any external databases. When combined with the Masked Built-up Extraction Index (MBEI), the proposed approach enables robust, unsupervised classification applicable even in data-scarce environments.

Fractal objects can be analyzed using deep learning algorithms that automatically extract features from high-dimensional data. Some related works in the literature use deep learning to identify the parameters of dynamical systems driven by fractional Brownian motion (FBM). Deep learning models have been used to estimate the Hurst exponent of FBM (Granik, Weiss, and Nehme 2019), to identify the parameters of nonlinear dynamical systems driven by FBM (Hou and Ma 2025), and to estimate the fractal dimension of the basins of attraction of the Duffing oscillator (Valle, Wagemakers, and Daza 2022). While Deep Learning-based methods achieve high accuracy, they require significant computational resources and large annotated datasets. In this work, we develop a computationally efficient, unsupervised alternative complementary to deep learning. Our method provides interpretable physical metrics (Fractal Dimension and Density) without needing extensive training phases as SpectralGPT, making this method particularly attractive for rapid assessments in data-scarce scenarios.

A deep neural network – particularly convolutional networks – that enables the automatic estimation of the fractal dimension of urban environments from multispectral imagery, which provides an effective tool for quantifying and classifying the morphological complexity of cities, has been implemented by us (Jimenez, Quitl, and Vallejo 2025). The CNN model was trained on a large synthetic dataset with a known ground-truth baseline to demonstrate its potential for transfer to real-world images. It has been trained on $128 \times 128$ synthetic bi-dimensional surfaces. To analyze high-resolution images and improve fractal estimation accuracy, the CNN model must be trained on synthetic and satellite images of larger sizes ($512 \times 512$, $1024 \times 1024$ pixels) thus also the interest of this work.

The manuscript is organized as follows: Section 2 (Definitions and Methods) describes concepts and main computational steps of the Detrended Moving Average (DMA) and the Masked Built-up Extraction Index (MBEI); in Section 3 (Data and Results), the main features of the Worldview-2 satellite images are illustrated. The fractal dimension $D_f$ is estimated for different urban and suburban images of 28 European cities. The built-up density $\mathcal{B}$ is quantified over binarized built-up maps of the same data. In Section 4 (Discussion), features corresponding to clusters with different urbanization levels for 112 sub-urban sectors in binarized maps are given. Conclusions and suggestions for future developments are presented in Section 5.

## 2. Definitions and methods

### 2.1. Fractal dimension $D_f$

The property of invariance under iteration describes the concept at the core of fractal geometry and self-similarity, which describes irregular structures, fragmented shapes, and real-world features that traditional geometry cannot grasp. Self-similar textures are characterized by scaling relations of the form:

$$f(\lambda) \propto \lambda^{D_f}, \tag{1}$$

with $\lambda$ a characteristic scale, a measuring unit size, and $D_f$ the fractal (Hausdorff) dimension:

$$D_f = d - H, \tag{2}$$

with $d$ the Euclidean dimension and $H \in \{0, 1\}$ the Hurst exponent that characterizes roughness and correlation degree. $H > 0.5$, $H < 0.5$, and $H = 0.5$ refer respectively to positive correlation, negative correlation, and lack of correlation. Fractional Brownian fields, i.e. continuous functions of two variables $f_H(x_1, x_2)$, with the Hurst exponent $H$ a parameter, can be adopted for studying irregular surfaces and structures.

### 2.2. Detrending moving average algorithm (DMA)

The DMA algorithm operates via a generalized high-dimensional variance $\sigma_{DMA}$ of $f_H(r)$ around the moving average function $\widetilde{f}_H(r)$. For $d = 2$, it writes (see (Carbone 2007) for further details):

$$\sigma^2_{DMA} = \frac{1}{(N_1 - n_{1_{max}})(N_2 - n_{2_{max}})} \sum_{i_1=n_1}^{N_1} \sum_{i_2=n_2}^{N_2} \left[ f(i_1, i_2) - \widetilde{f}_{n_1 n_2}(i_1, i_2) \right]^2, \tag{3}$$

$$\text{with} \quad \widetilde{f}_{n_1 n_2}(i_1, i_2) = \frac{1}{n_1 n_2} \sum_{k_1=0}^{n_1-1} \sum_{k_2=0}^{n_2-1} f(i_1 - k_1, i_2 - k_2). \tag{4}$$

The average field $\widetilde{f}_{n_1 n_2}(i_1, i_2)$ and the difference $f(i_1, i_2) - \widetilde{f}_{n_1, n_2}(i_1, i_2)$ are estimated over the sub-arrays with size $n_1 \times n_2$. It can be shown that for fractal fields, Equation (3) obeys the scaling relationship:

$$\sigma^2_{DMA} \sim \left[\sqrt{n_1^2 + n_2^2}\right]^{2H} = s^H, \tag{5}$$

with $s = n_1^2 + n_2^2$. Equation (3) can be implemented on matrices mapping bi-dimensional images with different resolutions. Then, a log-log plot of $\sigma^2_{DMA}$ as a function of $s$ would yield a straight line with slope $H$. As stated in Carbone (2007), deviations at large scales are caused by finite-size effects, occurring when the analyzed surfaces do not contain a sufficient amount of data for a statistically significant evaluation of the scaling law at large values of the moving average window $n$. Such finite-size effects become negligible for $n_{1,max} \ll N_1$, $n_{2,max} \ll N_2$, with $N_1 \times N_2$ the maximum data size. In this work, the DMA method will be implemented on extended data sets of remotely sensed images of several cities. The Red Band has been chosen as the primary input for fractal dimension estimation, motivated by the fact that it is found quite universally in remotely sensed imagery, hence it could represent a comparison term of broader interest than bands specific only to World-View. The outcomes are reported in Section 3 and Appendices.

### 2.3. Masked built-up extraction indices (MBEI)

In remote sensing, spectral indices yielded by mathematical combinations of reflectances at different wavelength bands are widely used to quantify urban and land cover. The straightforward mathematical structure and low computational cost make extensive index-based analysis highly efficient in distinguishing built-up areas across various spatial and temporal scales. However, a persistent challenge is the spectral similarity between impervious and bare soil covers, which often leads to misclassification. Bare soil typically exhibits high reflectance in near-infrared wavelengths and low reflectance in the green. Indices to capture the spectral behavior of bare soil use SWIR2 and green bands. Standard approaches mainly rely on Short-Wave Infrared (SWIR) bands to identify bare soil (Chen, Van de Voorde, and Roberts 2021; Dutta, Rahman, and Paul 2020; Nguyen, Chidthaisong, and Kieu Diem 2021).

Copernicus and WorldView imagery feature different spectral combinations. WorldView-2 (WV-2) imagery lacks the SWIR bands, while featuring a unique set of high-resolution bands, such as Coastal Blue, Yellow, and Near-Infrared 2 (NIR2). Therefore, specific indices tailored to these spectral components are required to accurately differentiate among reflectance values and suppress bare soil noise (Adeyemi, Ramoelo, and Cho 2021).

The Normalized Built-up Extraction Index (NBEI):

$$\text{NBEI} = \frac{(\text{NIR2} + \text{NIR1}) - (\text{Green} + \text{Red_edge})}{(\text{NIR2} + \text{NIR1}) + (\text{Green} + \text{Red_edge})}, \tag{6}$$

delineates built-up cover from WV-2 multispectral satellite images.

Built-up indices face limitations in accurately distinguishing constructed surfaces from bare soil or exposed rock, due to spectral similarities between these land covers, leading to overestimates of built-up areas. Such a limitation can be mitigated by using a mask to identify and exclude pixels corresponding to bare surfaces (Sun, Chen, and Jia 2015). To enhance the difference between impervious constructed

surfaces from bare soil and mitigate the risk of overestimating built-up areas, we put forward a masking technique specifically designed for the WV-2 spectral features as follows. To classify bare soil pixels, we define the World-View Soil Index (WVSI) as:

$$\mathrm{WVSI} = \frac{\mathrm{NIR2} - \mathrm{Green}}{\mathrm{NIR2} + \mathrm{Green}} \quad . \tag{7}$$

Both the *NBEI* and *WVSI* maps are computed over the same region of the multispectral dataset. Then, pixels with a high soil probability are identified via the *WVSI* and excluded from the built-up areas detected by the *NBEI*. This exclusion is operated by the *built-up mask* $\overline{M}$ defined for a pixel $(i_1, i_2)$ as:

$$\overline{M}\,(i_1, i_2) = \begin{cases} 0 & R_{min} < \mathrm{NBEI}(i_1, i_2) < R_{max} \\ & T_{min} < \mathrm{WVSI}(i_1, i_2) < T_{max} \\ 1 & \text{otherwise} \end{cases} , \tag{8}$$

$[R_{min}, R_{max}]$ is the *Soil Exclusion Range* and $[T_{min}, T_{max}]$ is the *Soil Detection Range*, i.e. the spectral thresholds for the NBEI and WVSI indices, respectively.

Next, the preliminary binarized map $B_0$ is generated from the NBEI index, which still retains misclassified pixels corresponding to bare soil due to the spectral overlap described earlier. $B_0$ is defined as:

$$B_0\,(i_1, i_2) = \begin{cases} 1 & \text{if } U_{\min} < \mathrm{NBEI}\,(i_1, i_2) < U_{\max} \\ 0 & \text{otherwise} \end{cases} , \tag{9}$$

$[U_{\min}, U_{\max}]$ is the *Built-up Acceptance Range*, i.e. the threshold valid for identifying built-up structures.

The threshold ranges $[R_{min}, R_{max}]$, $[T_{min}, T_{max}]$, $[U_{\min}, U_{\max}]$ are rigorously determined through an optimization algorithm based on structural similarity to maximize the separation between classes. The methodology for quantifying these optimal thresholds is discussed in Section 3.3 and fully detailed in Appendix B.

The Masked Built-up Extraction Index (*MBEI*) is obtained by strictly excluding the identified bare soil pixels from the initial classification. This is achieved by applying the built-up mask $\overline{M}$ to the preliminary *NBEI* map $B_0$, as follows:

$$B = B_0 \circ \overline{M} \quad , \tag{10}$$

where the symbol $\circ$ indicates the element-by-element product (Hadamard product) of the two matrices. This operation ensures that only pixels consistent with impervious materials are retained. Next, the morphological closing operation is applied to restore the spatial integrity of partially eroded urban structures. This step fills gaps caused by the noise added during the masking process while also preserving the structural boundaries of the urban zones:

$$MBEI = (B \oplus b) \ominus b, \tag{11}$$

where the symbols $\oplus$ and $\ominus$ denote dilation and erosion, respectively. The structuring element $b$ is defined as a disk with a radius $r$ proportional to the spatial resolution of the imagery, approximately covering the minimal structural unit of a building.

Finally, the normalized built-up density $\mathcal{B}$ quantifies the spatial concentration of urban development within the region of interest (Boyko and Cooper 2011):

$$\mathcal{B} = \frac{1}{A_{tot}} \sum_{i_1=1}^{M} \sum_{i_2=1}^{N} MBEI\ (i_1, i_2) \quad , \tag{12}$$

where $M$ and $N$ represent the dimensions of the image in pixels, and $A_{tot}$ is the total number of pixels defined as $A_{tot} = M \times N$. This metric provides a scale-independent value ranging from 0 to 1, enabling comparison between different cities.

In this subsection, the issue of defining built-up and soil indices appropriate for the WV-2 high-resolution imagery spectral components has been addressed. Furthermore, a masking procedure leading to the definition of the *MBEI* index is needed to overcome limitations and accurately distinguish between constructed surfaces and bare soil or exposed rock, due to spectral similarities among these land covers, leading to overestimates of built-up areas. To further optimize the built-up extraction algorithm, threshold ranges of the built-up mask are defined for the images in the dataset during the segmentation task.

## 3. Data and results

### 3.1. Worldview-2 satellite imagery dataset

Images of 28 European cities, processed by the European Space Imaging GmbH from February 2011 to October 2013, referred to as the *Urban Atlas*, are analyzed (UrbanAtlas 2021). The selected WorldView-2 imagery satisfies the criterion to have been recorded with atmospheric haze below 10% during spring. Regarding the vegetation phenology issue, this period of the year ensures that most of the vegetation emits within the green band, thus they are clearly distinguishable from the brown/red color of bare soil and construction, effectively ensuring the maximum selectivity of the MBEI index. The location of the 28 cities is shown in the map of Figure 1. The main features of the WorldView-2 spectral imagery are summarized in Table 1.

Satellite images cover an area of $134,\ 560\ \text{km}^2$ as yield respectively at high and low resolutions with pixel sizes of $1.6\ \text{m}\ \ (1.6\ \text{m} \times 7250\ \text{px})^2 = 134,\ 560\ \text{km}^2$ and of $10.73\ \text{m}$ yields $(10.73\ \text{m} \times 1080\ \text{px})^2 = 134,\ 560\ \text{km}^2$, respectively.

As a case study, the image WV-2 N50-774 (Brussels) is shown in Figure 2a. The false color image, obtained by combining the (Green + Red edge), NIR1, and NIR2 bands of the N50-774 WV-2 image, is shown in Figure 2b. The images are divided into four sub-images with sizes $540 \times 540$ pixels and $3625 \times 3625$ pixels at low and high resolution, respectively. The sub-images, delimited by yellow lines, are labeled by A, B, C, and D. Further WV-2 images of the WorldView-2 collection are shown in the following sections and in Appendix A.

### 3.2. Fractal dimension analysis

Hurst exponent $H$ and fractal dimension $D_f$ of the WorldView-2 (WV-2) images are obtained by using the two-dimensional *DMA* method summarized in subsection 2.2. The *DMA* algorithm has been implemented on squared windows with $n_1 = n_2$ according to Equations (3)–(5). The DMA is evaluated on each sub-image to get the variability of the scaling exponents for the different urban areas. For *high-resolution* images, $n_1 \in [14, 350]$ and $\Delta n_1 = 7$ have been used. Regressions are estimated in the range $(6 < s < 12.5)$, providing Hurst exponent values labeled by $H_1$ (Figure 3a). For *low-resolution* images, $n_1 \in [2, 49]$ and $\Delta n_1 = 1$ have been used. Regressions are estimated in the range $(2 < s < 8.5)$, providing Hurst exponent values labeled by $H_2$ (Figure 3b).

The DMA regressions with the corresponding values of $H_1$ and $H_2$ are shown in Figure 3 for the N50-774 (Brussels) sub-image A, B, C, and D. The Hurst exponents range between $0.12 \div 0.22$. As can be noted by

**Table 1.** World View-2 multispectral imagery characteristics.

| WV-2 database | Band | Wavelength(nm) |
|---|---|---|
| Low resolution | Red | 630–750 |
| (10.73 m/px) | Green | 500–620 |
| RoI 1080 × 1080 px | Blue | 400–500 |
| High resolution (1.60 m/px) RoI 7250 × 7250 px | Coastal Blue | 400–450 |
| | Blue | 450–510 |
| | Green | 510–580 |
| | Yellow | 585–625 |
| | Red | 630–690 |
| | Red Edge | 705–745 |
| | NIR 1 | 770–895 |
| | NIR 2 | 860–1040 |

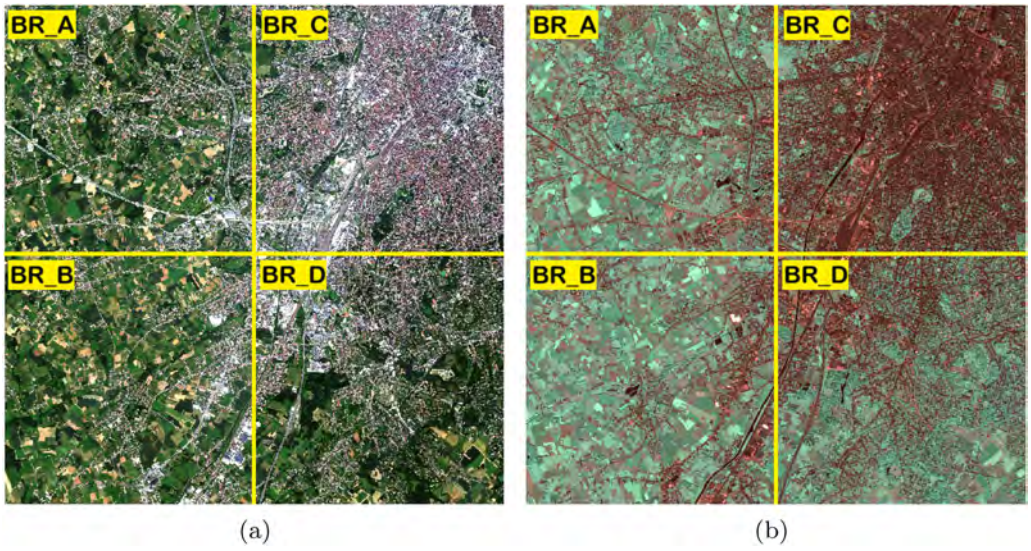


**Figure 2.** (a) Image N50-774 (Brussels) downloaded from the *Urban Atlas* collection of the largest European Cities of WorldView-2 (UrbanAtlas 2021). (b) False color image: buildings and roads are in orange, gardens, and forestlands are in cyan. Each RoI spans diverse land-use patterns, ranging from densely constructed city centers to peripheral vegetated zones.

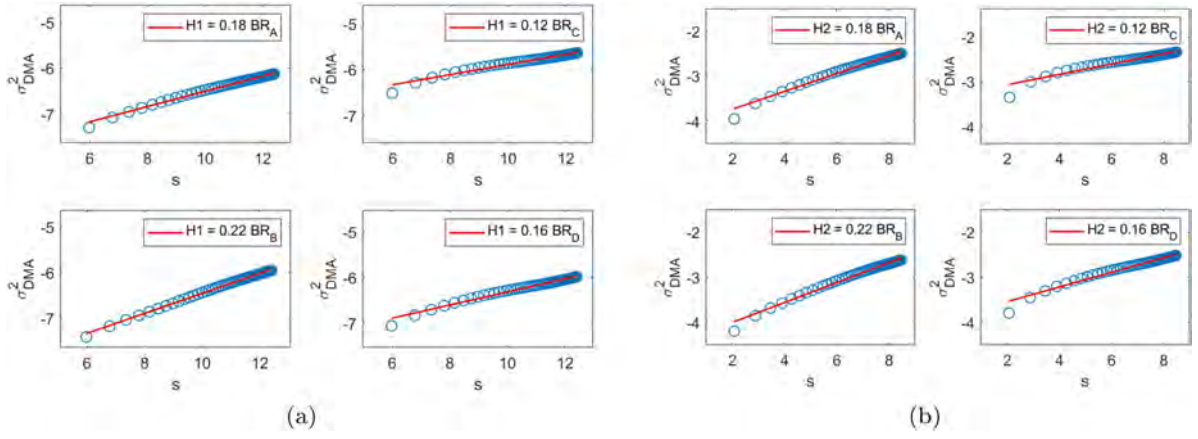


**Figure 3.** (a) Log-log plots of $\sigma^2_{DMA}$ for each high-resolution sub-image of size 3625 × 3625 pixels. Estimated values of $H_1$ are obtained as the slope of the regression line by least squares. (b) Log-log plots of $\sigma^2_{DMA}$ for each low-resolution sub-image of size 540 × 540 pixels. Estimated values of $H_2$ are obtained as the slope of the regression line by least squares.

comparing the four panels in Figures 2 and 3, Section C is highly urbanized, with a high concentration of buildings and infrastructures. Section D shows intermediate urbanization levels, while Sections A and B are the least urbanized areas. The Hurst exponent tends to be lower for urbanized areas, while its value increases for dispersed areas, providing insights into the variation of urban and sub-urban sectors.

Similarly to what was done for the city of Brussels, the urban fractal dimension has been estimated for a total of 28 WV-2 satellite images of European cities (the results of which can be found in the following sections and in Figures A1–A6 of the Appendix A). The extensive analysis has allowed us to verify the precision and robustness of the Hurst exponent estimation over the different *RoI* areas and pixel resolutions. Overall, the fractal dimension is highly robust for the same area at different pixel resolutions. Different urbanization levels are found with fractal dimension $D_f$ varying in the range $1.7 \div 1.9$. High $D_f$ values correspond to more densely populated areas and larger built-up surfaces. Suburban zones with a mix of urban and green areas are characterized by intermediate values of the fractal dimension. Peripheral

areas with low population density and limited urban development are characterized by minimal infrastructure and open land zones; fractal dimension values are close to the minimum. The fractal dimensions $D_f$ for the four sub-sectors of the 28 European cities are given in Table 2.

Figure 4(a) and (b) show the frequency of occurrence of the fractal dimension values for the 112 sub-urban sectors of the 28 European cities. The abscissas range between $D_f$ = 1.70 and $D_f$ = 1.90. The maximum frequency is found for fractal dimension close to $D_f$ = 1.87, indicating that the analyzed regions are mainly urbanized as could be reasonably expected for a collection of large cities.

The robustness of the DMA results has been assessed through parameter sensitivity of the Hurst exponent $H$. A core objective was to assess the sensitivity of the fractal dimension to different spatial resolutions and sensor properties. To this end, a comparison between WorldView-2 (WV-2) and Sentinel-

**Table 2.** Built-up density and fractal dimension ($D_f$) values for the high-resolution WorldView-2 images of 28 European cities.

| Image | S | $\mathcal{B}$ | $D_f$ | Image | S | $\mathcal{B}$ | $D_f$ | Image | S | $\mathcal{B}$ | $D_f$ | Image | S | $\mathcal{B}$ | $D_f$ |
|---|---|---|---|---|---|---|---|---|---|---|---|---|---|---|---|
| | A | 0.41 | 1.83 | | A | 0.16 | 1.87 | | A | 0.26 | 1.89 | | A | 0.04 | 1.77 |
| Amsterdam | B | 0.48 | 1.86 | Athens | B | 0.53 | 1.88 | Berlin | B | 0.16 | 1.88 | Bern | B | 0.19 | 1.85 |
| N52-373 | C | 0.21 | 1.85 | N37-951 | C | 0.64 | 1.90 | N52-520 | C | 0.14 | 1.81 | N46-948 | C | 0.15 | 1.83 |
| | D | 0.41 | 1.87 | | D | 0.59 | 1.89 | | D | 0.07 | 1.84 | | D | 0.23 | 1.87 |
| | A | 0.22 | 1.85 | | A | 0.13 | 1.82 | | A | 0.67 | 1.89 | | A | 0.19 | 1.86 |
| Bratislava | B | 0.23 | 1.76 | Brussels | B | 0.11 | 1.78 | Bucharest | B | 0.39 | 1.86 | Copenhagen | B | 0.24 | 1.85 |
| N48-169 | C | 0.42 | 1.86 | N44-426 | C | 0.63 | 1.88 | N50-774 | C | 0.48 | 1.87 | N55-711 | C | 0.32 | 1.88 |
| | D | 0.25 | 1.80 | | D | 0.23 | 1.84 | | D | 0.19 | 1.80 | | D | 0.37 | 1.87 |
| | A | 0.22 | 1.85 | | A | 0.36 | 1.85 | | A | 0.14 | 1.81 | | A | 0.27 | 1.85 |
| Dublin | B | 0.43 | 1.86 | Helsinki | B | 0.26 | 1.82 | LaValetta | B | 0.06 | 1.81 | Lisbon | B | 0.28 | 1.84 |
| N53-334 | C | 0.46 | 1.88 | N60-167 | C | 0.22 | 1.80 | N35-899 | C | 0.45 | 1.86 | N38-716 | C | 0.43 | 1.86 |
| | D | 0.46 | 1.89 | | D | 0.27 | 1.83 | | D | 0.24 | 1.83 | | D | 0.40 | 1.87 |
| | A | 0.05 | 1.82 | | A | 0.24 | 1.82 | | A | 0.12 | 1.81 | | A | 0.18 | 1.83 |
| Ljubljana | B | 0.32 | 1.85 | London | B | 0.14 | 1.80 | Luxembourg | B | 0.14 | 1.82 | Madrid | B | 0.36 | 1.84 |
| N46-056 | C | 0.05 | 1.84 | N51-509 | C | 0.18 | 1.82 | N49-611 | C | 0.16 | 1.83 | N40-331 | C | 0.50 | 1.88 |
| | D | 0.08 | 1.83 | | D | 0.30 | 1.87 | | D | 0.34 | 1.85 | | D | 0.48 | 1.85 |
| | A | 0.54 | 1.88 | | A | 0.28 | 1.87 | | A | 0.15 | 1.81 | | A | 0.19 | 1.88 |
| Milano | B | 0.46 | 1.86 | Nicosia | B | 0.29 | 1.88 | Oslo | B | 0.25 | 1.89 | Paris | B | 0.09 | 1.79 |
| N45-419 | C | 0.60 | 1.90 | N35-172 | C | 0.58 | 1.90 | N59-913 | C | 0.20 | 1.84 | N48-845 | C | 0.32 | 1.89 |
| | D | 0.42 | 1.87 | | D | 0.35 | 1.86 | | D | 0.26 | 1.87 | | D | 0.21 | 1.89 |
| | A | 0.22 | 1.82 | | A | 0.26 | 1.86 | | A | 0.34 | 1.86 | | A | 0.09 | 1.81 |
| Prague | B | 0.27 | 1.84 | Rome | B | 0.15 | 1.81 | Stockholm | B | 0.15 | 1.81 | Tallinn | B | 0.06 | 1.84 |
| N50-090 | C | 0.33 | 1.85 | N41-863 | C | 0.44 | 1.90 | N59-329 | C | 0.41 | 1.85 | N59-437 | C | 0.31 | 1.86 |
| | D | 0.48 | 1.86 | | D | 0.40 | 1.88 | | D | 0.36 | 1.87 | | D | 0.09 | 1.83 |
| | A | 0.56 | 1.88 | | A | 0.43 | 1.87 | | A | 0.27 | 1.86 | | A | 0.11 | 1.79 |
| Torino | B | 0.54 | 1.87 | Vienna | B | 0.61 | 1.88 | Vilnius | B | 0.09 | 1.83 | Zurich | B | 0.35 | 1.88 |
| N45-024 | C | 0.38 | 1.87 | N48-181 | C | 0.36 | 1.85 | N54-687 | C | 0.05 | 1.85 | N47-377 | C | 0.25 | 1.81 |
| | D | 0.11 | 1.82 | | D | 0.25 | 1.80 | | D | 0.01 | 1.82 | | D | 0.20 | 1.87 |

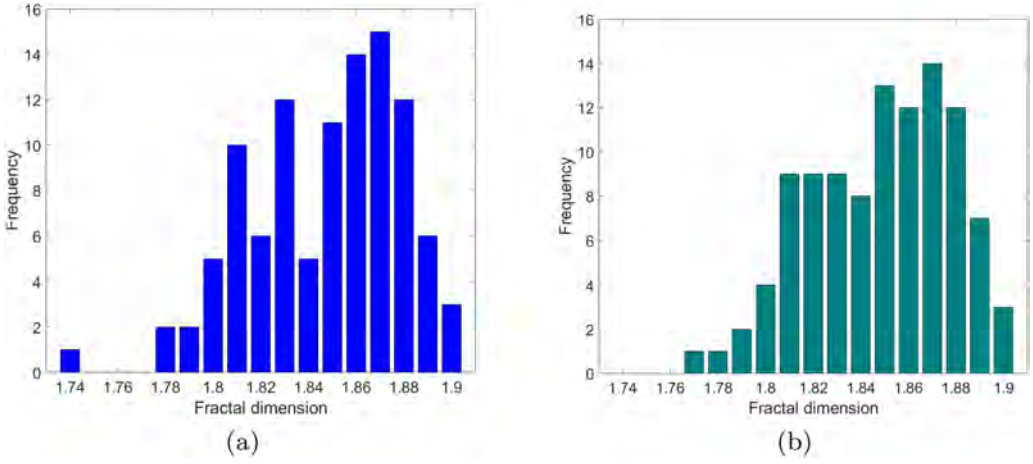


**Figure 4.** Histogram of the $D_f$ values of the 28 analyzed European cities for (a) low resolution and (b) high resolution imagery.

2 (S-2) was performed on identical ROIs, with WV-2 data for a direct comparison. While $H$ values differed between sensors due to spatial resolution, spectral properties, and temporal gap between acquisitions (WorldView-2 from 2011 vs. Sentinel-2 from 2025), the relative ranking of complexity across the four ROIs remained consistent (e.g. areas with higher $H$in WV-2 also showed higher $H$in S-2). This indicates the DMA method's robustness in discerning relative textural patterns despite data source differences. Furthermore, the fractal dimension ranges obtained for Vienna (1.76 ÷ 1.84), Prague (1.81 ÷ 1.84), and Zurich (1.75 ÷ 1.83), as a few samples ranked consistently above 1.7, reflect the high morphological complexity of these urban cores.

### 3.3. Built-up density

In this section, the built-up density $\mathcal{B}$ is estimated for diverse urban and sub-urban areas according to the methodology defined in Section 2.3. The built-up areas are extracted from the 112 sub-images of size $3625 \times 3625$ pixels of the 28 cities of the WorldView-2 high-resolution multispectral imagery. Each sub-image covers an area of approximately 33.64Km$^2$, displaying multiple land covers including built-up, bare soil, water bodies, and vegetation. First, the *NBEI* and *WVSI* maps were computed for all images using Equations (6) and (7), respectively. To ensure robust discrimination of built-up areas, the spectral threshold ranges ($R_{min}$, $R_{max}$), ($T_{min}$, $T_{max}$), in Equation (8) and ($U_{min}$, $U_{max}$) in Equation (9) were determined by the optimization algorithm detailed in Appendix B.

As observed in Figure 5a, the NBEI distribution exhibits overlap between built-up and bare soil areas, making a single index insufficient for accurate segmentation. Figure 5b shows the WVSI distribution with a wider threshold for bare soil.

Figure 6 qualitatively visualizes the method operating on the image of Brussels. A pixel ($i_1$, $i_2$) identified as bare soil in the *WVSI* map (Figure 6b) is removed from the *NBEI* map (Figure 6a) using the *built-up mask* $\overline{M}$ defined by Equation (8).

The final segmentation is achieved by applying the morphological closing operation (Equation (11) to the masked map. The resulting MBEI map for Brussels is presented in Figure 7. Based on the MBEI map, the normalized built-up density $\mathcal{B}$ was calculated for the four sub-sectors to quantify urbanization levels. The results highlight clear structural distinctions: the highly urbanized sub-sector C exhibits the maximum density ($\mathcal{B}_C = 0.63$), while the peripheral sub-sector D shows intermediate density ($\mathcal{B}_D = 0.23$). Conversely, sub-sectors A and B, characterized by dispersed structures, exhibit significantly lower density values ($\mathcal{B}_A = 0.13$ and $\mathcal{B}_B = 0.11$, respectively).

The density estimation methodology described here for Brussels was systematically implemented on the full dataset of 28 cities. Further details regarding robustness and accuracy of the methodology are illustrated in Appendix B and Figures B, B2, and B3. The same values of optimized spectral thresholds

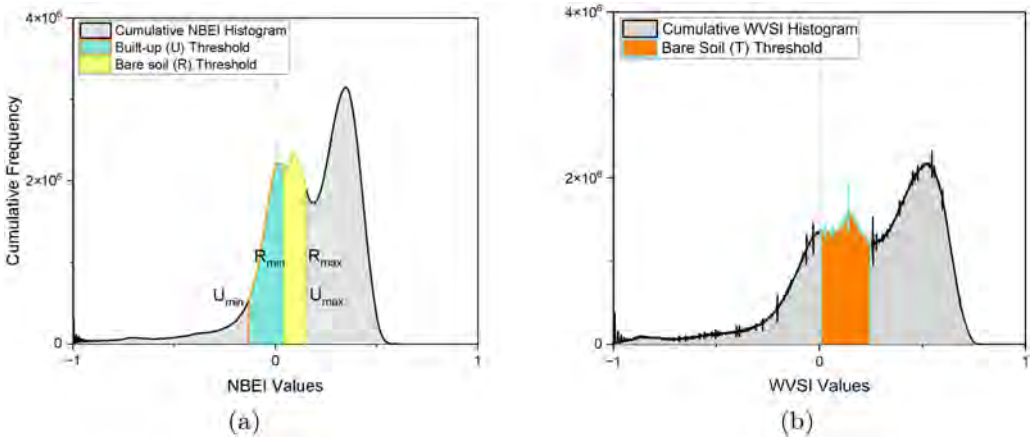


**Figure 5.** Cumulative histograms from (a) *NBEI* and (b) *WVSI* maps. The optimized threshold values shown in panel (a) are $R \in [0.0395, 0.149]$ and $U \in [-0.13, 0.149]$, while those shown in panel (b) are $T \in [0.048, 0.245]$.

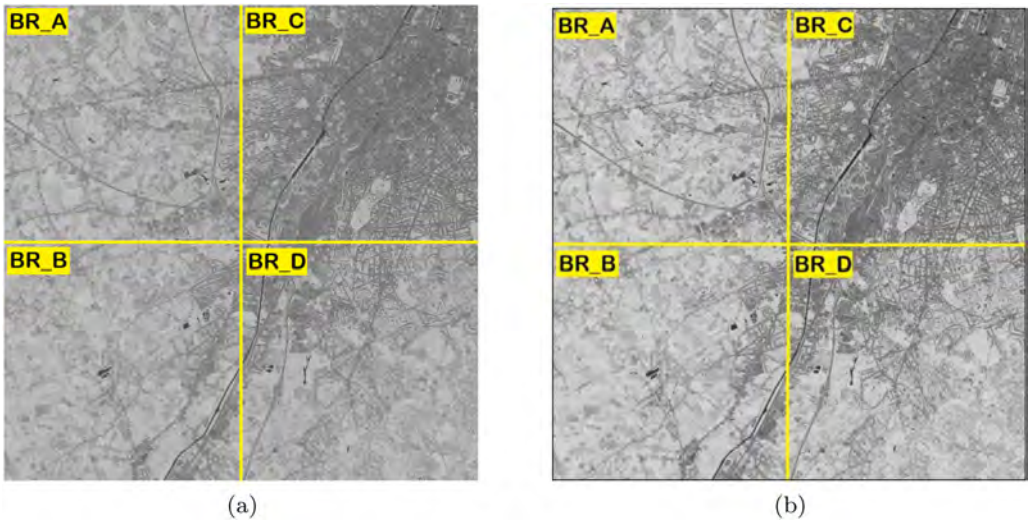


**Figure 6.** (a) *NBEI* and (b) *WVSI* maps obtained from Image N50-774 of Brussels city. A bare soil pixel $(i_1, i_2)$ belonging to the *WVSI* map is identified and removed from the *NBEI* map using the *built-up mask* $\overline{M}$ defined by (8)

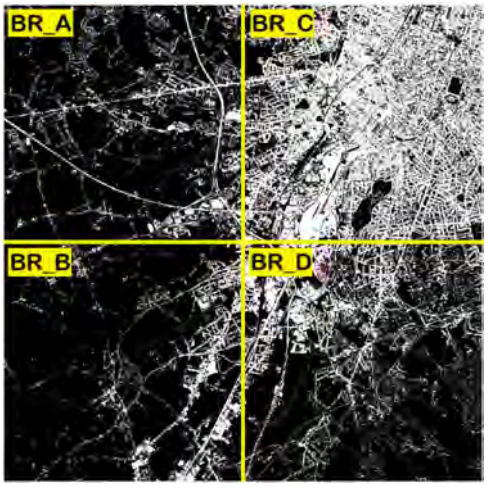


**Figure 7.** *MBEI* map is obtained according to the computational procedure defined by Equation (11), namely a closing operation using a disk-shaped structure element $b$ with a radius of 2 pixels. The map provides the pixels classified as urbanized in the N50-774 high-resolution image of Brussels city. Density values of the sub-urban sectors $\mathcal{B}_A = 0.13$, $\mathcal{B}_B = 0.11$, $\mathcal{B}_C = 0.63$, and $\mathcal{B}_D = 0.23$. One can note that the highly urbanized sub-sector C exhibits the maximum density value, the sub-sector D exhibits intermediate built-up density, and sub-sectors A and B have lower built-up density values.

$(R, T, U)$, derived in Appendix B were applied to all images without local retuning. The use of these globally optimized parameters ensures a consistent evaluation standard, verifying that the proposed method is robust enough to handle the spectral variability of different urban environments across various European cities.

## 4. Discussion

The urbanization variability has been quantified in terms of built-up density $\mathcal{B}$ and fractal dimension $D_f$ on 28 European cities multispectral satellite image collection of the WorldView-2 (WV-2) database. Specifically, a given feature $\mathbf{x} = (D_f, \mathcal{B})$ is used to classify the urbanization degree from highly dispersed to highly urbanized areas. By comparing these features, the variety of the urban contexts, e.g. due to

historical development, land use patterns, and social organization can be monitored over multiple spatial and temporal scales.

As reported in Section 3, the *DMA* algorithm is implemented on each sub-image to grasp the scaling properties of the urban and sub-urban areas. Table 2 shows the features $\mathbf{x} = (D_f, \mathcal{B})$ for the sub-sectors $S = (A, B, C, D)$ of the 28 cities.

The urban feature $\mathbf{x} = (D_f, \mathcal{B})$ are plotted in Figure 8 for the 28 cities. $D_f$ is highly robust up to two decimal places for both low and high-resolution images. As the resolution increases, the sensitivity of the DMA also increases; however, the difference in values remains minimal. The accuracy of the DMA and the MBEI analysis, dependent on multispectral bands of WorldView-2 imagery, has been previously analyzed in (Carbone, Murialdo, and Pieroni 2022; Toxqui, Padilla, and Delgadillo 2025). In these works, it has been shown that the fractal dimension takes consistent values across the eight bands given in Table 1. In accordance with these observations, the trend between urbanized and peripheral zones is predominantly described by the mean of these estimates, which is associated with the red band.

Thomas, Frankhauser, and Frenay (2010) propose an exponential relationship between density and fractality in a peri-urban context, namely $\mathcal{B} \approx e^{\beta D_f}$ to fit the features by using a nonlinear regression. Alternatively, linear, quadratic, and cubic regressions can be adopted. Regression classes and goodness of fit, evaluated as $R^2$, are shown in Table 3. In several cases, the quadratic and cubic relationships provide the best approximation, though the exponential model might still be preferable for its simplified mathematical representation.

The *MBEI* maps derived from the proposed spectral index are analyzed to estimate the urban fractal dimension. The results obtained by using the *DMA* are compared against the Box Counting (BC). Figure 9 plots the urban features $\mathbf{x} = (D_f, \mathcal{B})$ of Brussels with the fractal dimension estimated by the DMA and BC algorithm.

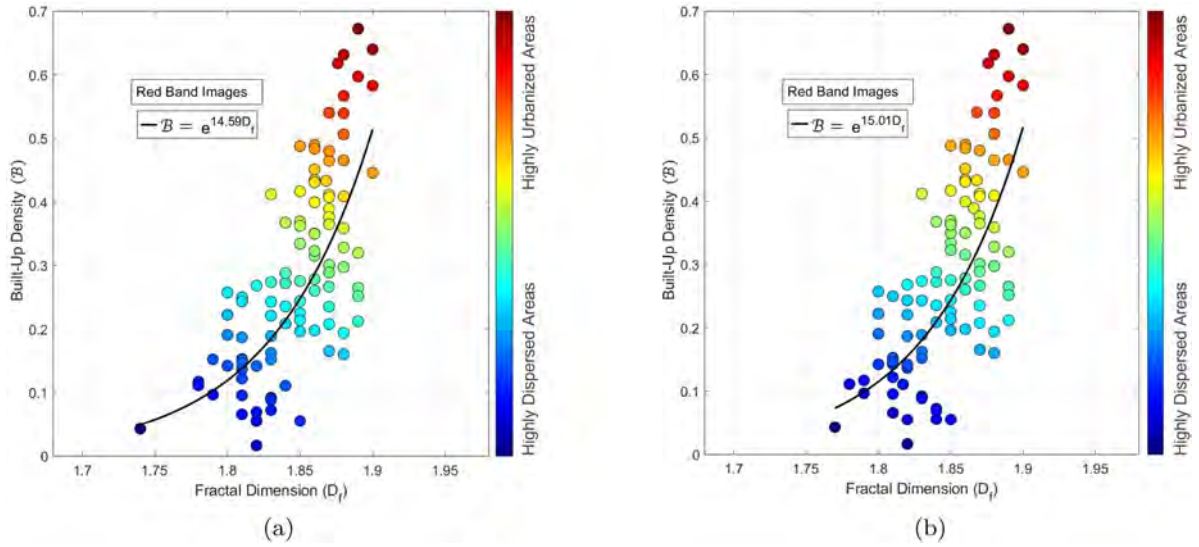


**Figure 8.** Urban feature space of built-up density $\mathcal{B}$ (derived from high-resolution imagery) and fractal dimension $D_f$ estimated from red bands of (a) low-resolution and (b) high-resolution imagery.

**Table 3.** $R^2$ values to quantify the fitting model.

| Regression models | Case 1 Figure 8(a) | Case 2 Figure 8(b) | Case 3 Figure 10(a) | Case 4 Figure 10(b) |
|---|---|---|---|---|
| Linear | 0.476 | 0.474 | 0.763 | 0.658 |
| Quadratic | 0.494 | 0.483 | **0.766** | **0.770** |
| Cubic | **0.495** | **0.485** | **0.766** | **0.770** |
| Exponential | 0.462 | 0.449 | 0.738 | 0.729 |

The bold values represent the optimal data fit for each regression model.

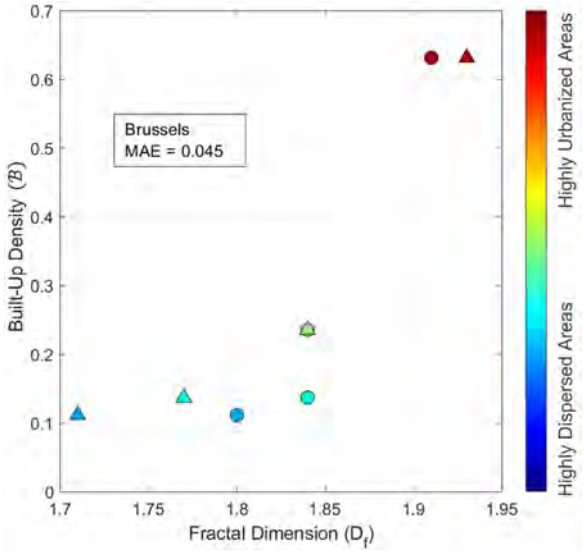


**Figure 9.** Built-up density $\mathcal{B}$ and fractal dimension $D_f$, respectively, obtained by the *DMA* (O) and *BC* (Δ) methods for Brussels.

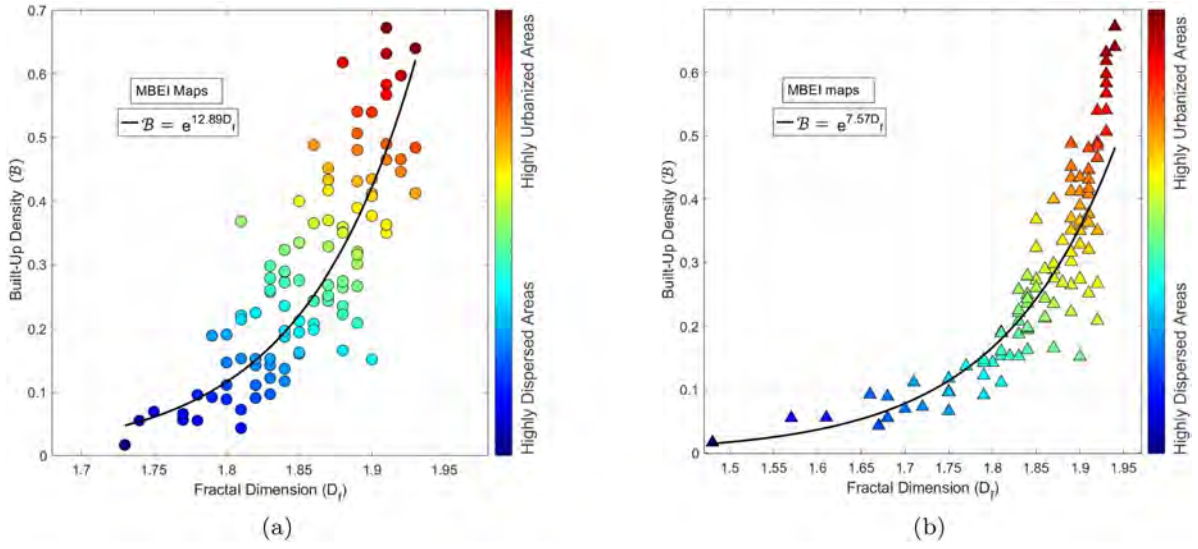


**Figure 10.** Urban feature space of built-up density $\mathcal{B}$ and fractal dimension $D_f$, estimated from *MBEI* maps of size 3625 × 3625 pixels using the (a) *DMA* and (b) *BC* for the 112 sub-urban sectors from European cities.

Figure 10 plots the urban features $\mathbf{x} = (D_f, \mathcal{B})$ estimated from sub-sectors of the *MBEI* maps. The symbol '○' corresponds to values estimated by using the *DMA*, whereas the symbol 'Δ' corresponds to values yielded by the Box Counting approach. The mean absolute error (MAE) quantifies the difference in the estimation of the fractal dimension $D_f$ by using either method. In both cases, high values of $\mathbf{x}$ indicate *dense built-up areas*, characterized by a high concentration of buildings and constructed surfaces. Low values of $\mathbf{x}$ are associated with *sparse built-up areas* characterized by minimal building structures, or large portions of undeveloped land covered by natural elements. Analogous results observed in the other analyzed cities can be found in Appendix A. An increase is observed in the range of the fractal dimension $D_f$, from $1.73 \div 1.93$ for *DMA* and $1.48 \div 1.94$ for *BC*. Despite the diverse morphologies, internal organization patterns, and types of spatial components across the satellite image dataset, we observe a robust correlation between fractal dimension $D_f$ and built-up density $\mathcal{B}$.

### 4.1. Clustering built-up density and fractal dimension

Built-up density and fractal dimension values are used to define clusters, i.e. images grouped according to the similarity degree of predefined urban features (Wang and Biljecki 2022). The instances of built-up density and fractal dimension are assigned to clusters corresponding to different levels of urbanization according to the *Minimum Volume Enclosing Ellipsoid (MVEE)* criterion (Van Aelst and Rousseeuw 2009).

Consider a set of $m$ urban features $m = \{\mathbf{x}_1, \mathbf{x}_2, \ldots, \mathbf{x}_{112}\} \in \mathbb{R}^2$, divided into $W = 4$ pattern clusters $\omega_1, \omega_2, \ldots, \omega_W$, based on the degree of urbanization (highly dispersed, dispersed, urbanized, and highly urbanized), as reported in (Carbone, Murialdo, and Pieroni 2022). Let us denote the Minimum Volume Enclosing Ellipsoid by $MVEE(m_W)$. The MATLAB function $MVEE(m_W)$ is used to determine the ellipsoid $\mathcal{E}_W$ with the smallest volume that surrounds the set of points $m_W$ at centroid $c_W$ (Moshtagh et al. 2005). If an unassigned point $m$ is contained in the ellipsoid $E_W$, the point $m$ is assigned to that cluster. For each cluster $w_W$, we compute the $MVEE(m_W)$ function for the points assigned to that cluster, as shown in Figures 11, C1, and C2.

The cluster features quantified by using the $MVEE(m_W)$ criterion are summarized in Table 4. The first column reports the cluster centroid $c_W$ and the number of points $|m_W|$ labeled. The second column reports the cluster features with the fractal dimension analysis estimated with DMA on red band images. Most urban features belong to cluster $w_2$. The third column reports the cluster features with the analysis performed with DMA on MBEI data. Given that the MBEI map highlights built-up features – and excludes vegetation, bare soil, water, and other non-urban elements, a greater concentration of urban features is found in cluster $w_3$. This refinement not only changes the cluster allocation but also alters the range of the calculated fractal dimension. In the fourth column, the clustering of the urban features corresponds to fractal dimensions obtained by the box-counting method. We observed that some isolated features (which correspond morphologically to hybrid sectors typically associated with urban variability, discontinuous urban expansion, or transitional urban areas) fall outside the range. These urban features were excluded only during the geometric construction of the $MVEE(m_W)$ boundaries for the box-counting results, while all of them were retained in the DMA analysis. Defining ellipses to encompass these outliers would lead to greater overlap between clusters, thereby deteriorating the selectivity of the approach. The distribution derived from DMA produced compact and well-separated clusters, allowing the $MVEE(m_W)$ to enclose all observations without overlap between urbanization classes. This behavior suggests that the DMA estimator provides a more stable representation of urban morphology for the clustering procedure. Figures 11(a-c) show the ellipsoids $E_W$ enclosing the urban features $\mathbf{x}$ for the 112 suburban sectors of the 28 European cities. Specifically, the features are estimated by using: the DMA algorithm on the red-band satellite images in Figure 11(a); the DMA algorithm on the *MBEI* maps in Figure 11(b); the Box Counting technique on the *MBEI* maps in Figure 11(c).

The centroids $c_W$ and the number $|m_W|$ of points enclosed in the clusters are given in Table 4. Box plots in Figure 12(a–c) show the distribution of $D_f$ values and skewness by displaying the data quartiles and averages. Overall, the wide set of results proves the discriminatory power of the selected urban features and their consistency across methods.

The implementation of the MBEI/DMA clustering has been mainly illustrated for the WV-2 Urban Atlas collection. The reason behind this choice is that Urban Atlas is a reference dataset adopted in many studies. Moreover, the analyzed cities have been established and fully developed for several centuries, thus their features have not changed significantly over the last few decades, when the satellite observations have been routinely implemented. Therefore, the obtained clusters can be easily used as a standard reference for different sectors within the same cities, among different cities, or eventually against other similar socio-demographic cluster features. Nonetheless, to ensure robustness and accuracy of the approach, additional data from the collection of WorldView ESA archive in the period 2017-2021 and Sentinel-2 L2A data from 2025 have been analyzed. Examples of such analysis are reported in Appendix C. As a further assessment, the Wilcoxon signed-rank test ($p < 0.049$) detected a statistically significant difference between spatial resolutions, and the Bland–Altman analysis demonstrated that the agreement between both measurements is very high. The mean bias between resolutions is close to zero, and nearly all observations fall within the

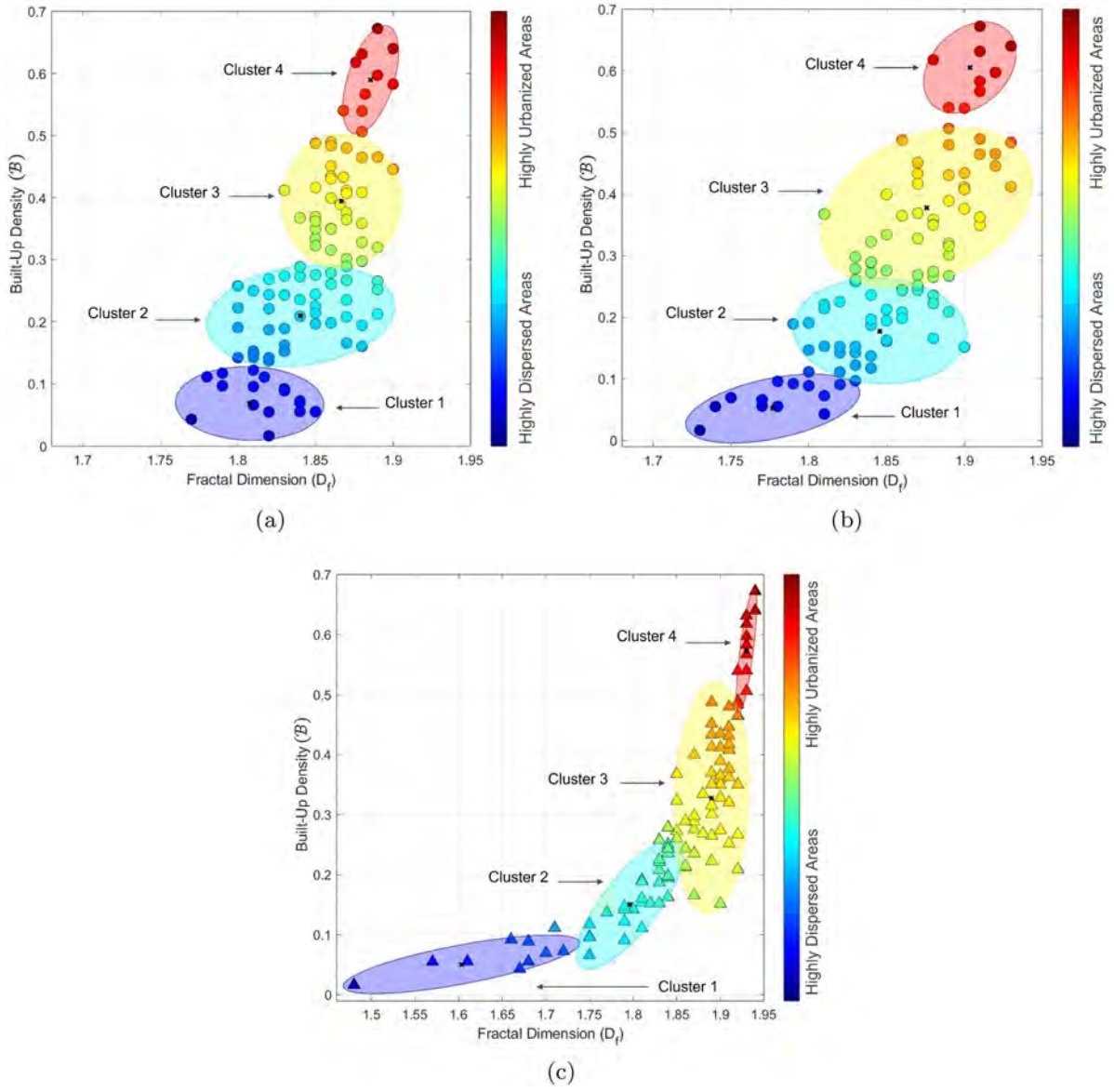


**Figure 11.** Built-up indices and fractal dimension clustered by means of the *MVEE* ($m_W$) algorithm. The features are estimated by implementing the *DMA* method on high-resolution red images in panel (a) and high-resolution *MBEI* maps (b). The clusters in panel (c) refer to features estimated by the Box Counting method on high-resolution *MBEI* maps.

**Table 4.** Centroids $c_W$ of ellipses $E_W$ enclosing $|m_W|$ points for each cluster $w_W$. The urban features are estimated by using high-resolution satellite images.

| Cluster $w_W$ | DMA (red image) | DMA (MBEI) | BC (MBEI) |
|---|---|---|---|
| $c_1$ | (1.80, 0.06) | (1.77, 0.05) | (1.60, 0.05) |
| $\|m_1\|$ | 17 | 13 | 9 |
| $c_2$ | (1.84, 0.20) | (1.84, 0.17) | (1.79, 0.15) |
| $\|m_2\|$ | **45** | 41 | 33 |
| $c_3$ | (1.86, 0.39) | (1.87, 0.37) | (1.89, 0.32) |
| $\|m_3\|$ | 38 | **47** | **53** |
| $c_4$ | (1.88, 0.58) | (1.90, 0.60) | (1.93, 0.57) |
| $\|m_4\|$ | 12 | 11 | 14 |

The bold values represent the largest number of urban features within the cluster.

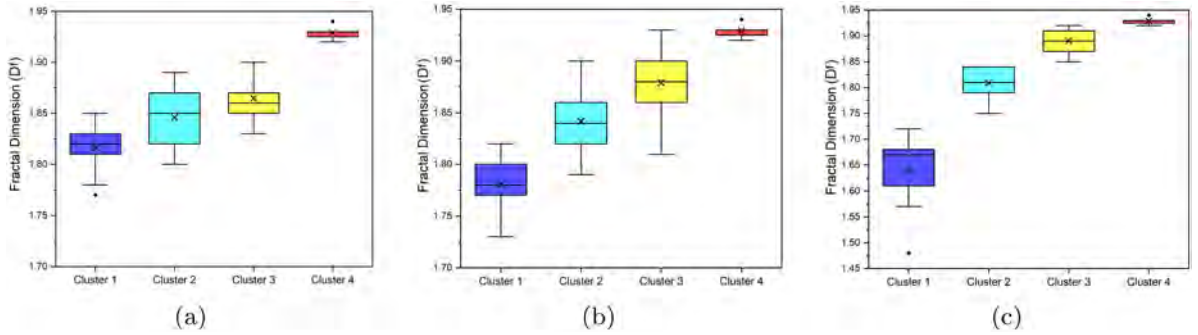


**Figure 12.** Box and Whiskers plots exhibiting the median (central bar) and inter-quartile range (between lower and upper bars) of the fractal dimension data across clusters. Features $D_f$ are estimated using (a) DMA (red images), (b) DMA (MBEI map), and (c) BC (MBEI map).

95% limits of agreement without any systematic trend across the measurement range. These results indicate that the differences introduced by spatial resolution are randomly distributed and remain small compared to the overall variability of the urban morphology, see Figure C4.

## 5. Conclusions

Morphology and built-up density are crucial indicators of complex urban systems. In this work, the variability of the urbanization degree is quantified in terms of the relation between built-up density $\mathcal{B}$ and fractal dimension $D_f$ on 28 European capital cities by using the WorldView2 multispectral satellite images.

The fractal dimension $D_f$ has been estimated by using the *DMA* on the red band images at two spatial resolutions. The results show that the $D_f$ values range between $1.74 \div 1.90$ at high $(1.6m/px)$ and low $(10.73m/px)$ spatial resolutions. This means that they remain almost invariant. Our results are consistent with previous studies (Thomas, Frankhauser, and Frenay 2010) and (Carbone, Murialdo, and Pieroni 2022), which report $D_f$ values around $1.8 \div 1.9$ for urbanized areas and $D_f$ values between $1.65 \div 1.9$ for different levels of urbanization, respectively.

The built-up density $\mathcal{B}$ has been estimated on the *MBEI* map obtained from high-resolution multispectral imagery. This map contains all image pixels classified as urban development with an accuracy higher than 83.42%. The binary *MBEI* map enhances impermeable surfaces, including buildings, houses, roads, asphalt, and other construction materials. The relevance of the implemented MBEI index lies in its ability to extract construction without including bare soil, unlike other built-up indices found in the literature.

Having developed the MBEI maps, the fractal dimension $D_f$ is estimated for urban and suburban sectors in the binary *MBEI* maps of size $[M \times N] = 7250 \times 7250$ and $[M/2 \times N/2] = 3625 \times 3625$ pixels, respectively. The variability of the scaling properties of different areas is analyzed. The fractal dimension $D_f$, estimated using the *DMA* and the Box Counting method, ranges from $1.74 \div 1.94$ for sub-urban and $1.8 \div 1.94$ for urban sectors. The $D_f$ ranges from $1.73 \div 1.93$ using the *DMA* and $1.48 \div 1.94$ using the Box Counting method.

The joint measure of built-up density and fractal dimension allows the definition of cluster features $E_W$ corresponding to $W$ levels of urbanization. $W = 4$ clusters feature the urban features $\mathbf{x}$ defined by the $MVEE(m_W)$ algorithm. The 112 suburban sectors from European cities are categorized into $W = 1$ (highly dispersed areas), $W = 2$ (dispersed areas), $W = 3$ (urbanized areas), and $W = 4$ (highly urbanized areas). We observe a greater concentration $|m_3| = 47$ of urban features $\mathbf{x} = (D_f\ (MBEI), \mathcal{B})$ in the Cluster $E_3$ corresponding to urbanized areas. This is due to the *MBEI* map of suburban sectors, which focuses specifically on built-up features, excluding vegetation, bare soil, water, and other non-urban elements. Box and Whisker plots measure the discriminatory power of urban features that remain consistent across methods. Even more, due to the accurate estimation of the fractal dimension using the *DMA* on the proposed *MBEI* map, clusters are well separated.

The example of Brussels allows us to show the type of morphology in the various sectors of our case study. It includes sub-sectors where the natural environment has been affected by urban sprawl. Sub-sectors with high built-up density $\mathcal{B}(C) = 0.63$ fall within the cluster $w_4$, which exhibits a high fractal dimension value $D_f = 1.88$. Approaching the cluster $w_1$, we observe that urban sprawl decreases with $D_f = 1.78$, and a natural environment $\mathcal{B}(B) = 0.11$ is observed. The clustering results are corroborated in the sub-sectors of other studied cities. As shown in Appendix A, we observe high built-up density in Athens, Rome, and Prague, with corresponding fractal dimension values consistent with the type of sub-sector analyzed. On the other hand, sub-sectors in Paris, Turin, and Zurich, with low urban sprawl, correspond to low fractal dimension values, thus confirming the validity of the clustering approach. A superlinear (exponential) relationship between urban features $\mathbf{x} = (D_f, \mathcal{B})$ is observed. It suggests that as built-up density increases, the complexity of the morphology increases more than linearly.

Unlike multi-modal classification approaches that require fusing satellite imagery with GIS or SAR data, our method extracts two complementary urban features (Fractal Dimension and Density) from a single input image. This ensures that the classification is not hindered by the lack of auxiliary data infrastructure. Integrating two distinct data features via Minimum Volume Enclosing Ellipsoids (MVEE) clustering enables a unique categorization of urban typologies that accounts for both the spatial arrangement (via DMA) and the density (via MBEI) of the built-up structures. Together, these elements underscore the novelty of our framework, which combines an enhanced spectral index, self-contained feature extraction from a single data source, and an unsupervised clustering strategy based on geometric compactness. We expect these technical advantages to support more accurate and generalizable assessments of urban morphology from optical satellite imagery.

To conclude, fractal dimension $D_f$ and built-up density $\mathcal{B}$ prove to be practical tools for identifying and characterizing different levels of urbanization. Both urban features are extracted from the same WV-2 imagery database. The proposed urban feature $\mathbf{x} = (D_f, \mathcal{B})$ allows the recognition of spatial patterns that reflect the complexity and density of the built environment. Unsupervised statistical methods group urban and sub-urban sectors into meaningful clusters based on their morphological features, offering a robust framework for comparative urban analysis.

The individual components of our approach (such as fractal dimension, built-up indices, and unsupervised clustering) are well-established in the literature. The novelty of our work lies in its unique integration, optimization, and application to solve a specific, persistent problem in remote sensing: the accurate, self-contained classification of urban morphology from a single data source. We have developed a custom built-up index that integrates an adaptive mask to explicitly and effectively discard bare soil pixels – a significant source of confusion that is often not addressed by standard indices. Furthermore, its operationalization using a generalizable, physically derived threshold (based on global band averages) represents a key advancement toward automated, scalable applications across diverse geographic contexts without site-specific tuning. The principal innovation is the derivation of two complementary, physically meaningful urban descriptors – morphological complexity ($D_f$) and physical density ($\mathcal{B}$) – from a single multispectral image without any auxiliary data. This integrated process transforms a standard optical image into a robust feature space for urban analysis, overcoming a critical dependency on external – and often unavailable – GIS or census layers. The novel combination of these two independently derived features ($D_f$ and $\mathcal{B}$) within a Minimum Volume Enclosing Ellipsoid (MVEE) clustering framework generates a new, interpretable classification of urban typologies. This fusion captures the interaction between the spatial arrangement and the material density of built-up areas – a synthesis not commonly found in methods that rely solely on spectral or morphological metrics. Our work provides novel, substantial methodological insight by creating a cohesive, optimized, and application-driven framework. This framework successfully bridges the gap between spectral signal processing and geospatial urban analysis, offering a reproducible tool for unsupervised urban characterization in data-scarce environments.

Finally, it is worth remarking on the existing limitations due to the heterogeneity of urban data sources and the static nature of many datasets, which fail to adequately capture temporal dynamics. To address this, we focus on extracting characteristic patterns directly from high-resolution satellite imagery, using unsupervised learning techniques to perform clustering. This approach enables the derivation of consistent

and comparable morphological and land-use indicators, partially overcoming the disparity in formats and lack of standardization in urban datasets. However, the approach is not free from the limitation that these spatial patterns primarily represent a single point in time. Future work will focus on evaluating the proposed MBEI index using new extended datasets acquired from other satellite sensors, such as WorldView-3 and Sentinel-2. In the mid-term, the proposed framework could be extended by incorporating models qualified to capture urban transitions and trajectories by employing Graph Neural Networks (GNNs) to model spatial relationships and analyze multi-temporal image series. The integration will significantly enhance the extraction and interpretation of complex spatio-temporal patterns. To address the limitation due to the scarcity of labeled data, *synthetic cities* yielded by generative models will be used as complementary data input. These will serve as a robust data bank for training, testing, and validating our clustering models, thereby improving generality and robustness.

## Acknowledgements

The authors thank the European Space Agency (ESA) for granting access to the WorldView satellite imagery to Politecnico di Torino. A. Aguilar-Vallejo (CVU No. 541295) and A. Delgadillo-Jimenez (CVU No. 1323784) express gratitude to the *Secretaría de Ciencias, Humanidades, Tecnología e Innovación* (SECIHTI) for the PhD scholarships. We also acknowledge support from the Government of the State of Hidalgo via the *Consejo de Ciencia, Tecnología e Inovación de Hidalgo* (CITNOVA) through the scholarship '*Becas de apoyo para estancias cortas de Maestría y Doctorado en Instituciones Nacionales y en el Extranjero*'.

## Author contributions

CRediT: **Armando Delgadillo-Jimenez:** Conceptualization, Data curation, Formal analysis, Investigation, Methodology, Validation, Writing – original draft, Writing – review & editing; **Carina Toxqui-Quitl:** Conceptualization, Data curation, Funding acquisition, Resources, Writing – original draft, Writing – review & editing; **Aldo Aguilar-Vallejo:** Conceptualization, Data curation, Formal analysis, Investigation, Methodology, Software, Validation, Writing – original draft, Writing – review & editing; **Alfonso Padilla-Vivanco:** Conceptualization, Data curation, Formal analysis, Funding acquisition, Investigation, Project administration, Resources, Supervision, Writing – original draft, Writing – review & editing; **Anna Carbone:** Conceptualization, Formal analysis, Funding acquisition, Investigation, Methodology, Project administration, Resources, Software, Validation, Writing – original draft, Writing – review & editing.

## Disclosure statement

No potential conflict of interest was reported by the author(s).

## Data availability statement

The data that support the findings of this research are available from the ESA repository at https://tpm-ds.eo.esa.int/oads/access/collection.

## References

Adeyemi, A., A. Ramoelo, M. Cho, and C. Masemola. 2021. "Spectral Index to Improve the Extraction of Built-Up Area from WorldView-2 Imagery." *Journal of Applied Remote Sensing* 15 (2): 024510.

Anestis, G., and D. Stathakis. 2024. "Urbanization Trends from Global to the Local Scale, *Geographical Information Science* 357–375. Elsevier.

Artmann, M., L. Inostroza, and P. Fan. 2019. "Urban Sprawl, Compact Urban Development and Green Cities. How Much Do We Know, How Much Do We Agree?

Arvidsson, M., N. Lovsjö, and M. Keuschnigg. 2023. "Urban Scaling Laws Arise from Within-City Inequalities." *Nature Human Behaviour* 7 (3): 365–374.

Batty, M., and P. A. Longley. 1987. "Fractal-Based Description of Urban Form." *Environment and Planning B: Planning and Design* 14 (2): 123–134.

Belgiu, M., L. Drăguţ, and J. Strobl. 2014. "Quantitative Evaluation of Variations in Rule-Based Classifications of Land Cover in Urban Neighbourhoods Using WorldView-2 Imagery." *ISPRS Journal of Photogrammetry and Remote Sensing* 87: 205–215.

Boyko, C. T., and R. Cooper. 2011. "Clarifying and Re-Conceptualising Density." *Progress in Planning* 76 (1): 1–61.

Carbone, A. 2007. "Algorithm to Estimate the Hurst Exponent of High-Dimensional Fractals." *Physical Review E—Statistical, Nonlinear, and Soft Matter Physics* 76 (5): 056703.
Carbone, A., P. Murialdo, A. Pieroni, and C. Toxqui-Quitl. 2022. "Atlas of Urban Scaling Laws." *Journal of Physics: Complexity* 3 (2): 025007.
Carbone, A., S. Luiz da Silva, and G. Kaniadakis. 2024. Capturing Urban Scaling Laws Via Spatio-Temporal Correlated Clusters. In *Urban Scaling*. Taylor & Francis.
Chen, F., T. Van de Voorde, D. Roberts, H. Zhao, and J. Chen. 2021. "Detection of Ground Materials Using Normalized Difference Indices with a Threshold: Risk and Ways to Improve." *Remote Sensing* 13 (3): 450.
Di Martino, G., A. Iodice, D. Riccio, G. Ruello, and I. Zinno. 2017. "The Role of Resolution in the Estimation of Fractal Dimension Maps from Sar Data." *Remote Sensing* 10 (1): 9.
Dong, L., Z. Huang, J. Zhang, and Y. Liu. 2020. "Understanding the Mesoscopic Scaling Patterns Within Cities." *Scientific Reports* 10 (1): 21201.
Dutta, D., A. Rahman, S. K. Paul, and A. Kundu. 2020. "Estimating Urban Growth in Peri-Urban Areas and Its Interrelationships with Built-Up Density Using Earth Observation Datasets." *The Annals of Regional Science* 65 (1): 67–82.
Esch, T., H. Asamer, F. Bachofer, J. Balhar, M. Boettcher, E. Boissier, and P. d' Angelo, et al. 2020. "Digital World Meets Urban planet–new Prospects for Evidence-Based Urban Studies Arising from Joint Exploitation of Big Earth Data, Information Technology and Shared Knowledge." *International Journal of Digital Earth* 13(1): 136–157. .
Fenta, A. A., H. Yasuda, N. Haregeweyn, A. S. Belay, Z. Hadush, M. A. Gebremedhin, and G. Mekonnen. 2017. "The Dynamics of Urban Expansion and Land Use/Land Cover Changes Using Remote Sensing and Spatial Metrics: the Case of Mekelle City of Northern Ethiopia." *International Journal of Remote Sensing* 38 (14): 4107–4129.
Frankhauser, P. 1998. "The Fractal Approach. a New Tool for the Spatial Analysis of Urban Agglomerations." *Population: An English Selection* 205–240.
Granik, N., L. E. Weiss, E. Nehme, M. Levin, M. Chein, E. Perlson, Y. Roichman, and Y. Shechtman. 2019. "Single-Particle Diffusion Characterization By Deep Learning." *Biophysical* 117 (2): 185–192. Journal.
Hendrick, M., A. Rinaldo, and G. Manoli. 2025. "A Stochastic Theory of Urban Metabolism." *Proceedings of the National Academy of Sciences* 122 (33): e2501224122.
Hou, W., and S. Ma. 2025. "Deep Learning for Parameter Identification of Nonlinear Dynamical System Driven By Fractional Brownian Motion." *Nonlinear Dynamics* 113 (16): 20667–20686.
Huang, L., J. Liu, Z. Sun, X. Li, N. Ishwaran, S. Lu, and Z. Xu, et al. 2024. "Perceiving Progress and Imbalance of Environmental SDG Indicators in China Using Big Data." *International Journal of Digital Earth* 17 (1): 2297847.
Jiao, L. 2015. "Urban Land Density Function: a New Method to Characterize Urban Expansion." *Landscape and Urban Planning* 139: 26–39.
Jimenez, A. D., C. T. Quitl, A. A. Vallejo, R. C. Ortega, A. P. Vivanco, and A. Carbone. 2025. Estimation of Urban Fractal Dimension Using a Convolutional Neural Network. In *Mexican International Conference on Artificial Intelligence*. 410–421. Springer.
Maxwell, A. E., T. A. Warner, and L. A. Guillén. 2021. "Accuracy Assessment in Convolutional Neural Network-Based Deep Learning Remote Sensing studies—part 1: Literature Review." *Remote Sensing* 13 (13): 2450.
Moreno-Monroy, A. I., M. Schiavina, and P. Veneri. 2021. "Metropolitan Areas in the World. Delineation and Population Trends." *Journal of Urban Economics* 125: 103242.
Moshtagh, N. 2005. "Minimum Volume Enclosing Ellipsoid." *Convex Optimization* 111 (January): 1–9.
Nguyen, C. T., A. Chidthaisong, P. Kieu Diem, and L.Z. Huo. 2021. "A Modified Bare Soil Index to Identify Bare Land Features during Agricultural Fallow-Period in Southeast Asia Using Landsat 8." *Land* 10 (3): 231.
Reia, S. M., P. S. C. Rao, M. Barthelemy, and S. V. Ukkusuri. 2022. "Spatial Structure of City Population Growth." *Nature Communications* 13 (1): 5931.
Ribeiro, F. L., and D. Rybski. 2023. "Mathematical Models to Explain the Origin of Urban Scaling Laws." *Physics Reports* 1012: 1–39.
Sameen, M. I., and B. Pradhan. 2016. "A Novel Built-Up Spectral Index Developed By Using Multiobjective Particle-Swarm-Optimization Technique." *IOP Conference Series: Earth and Environmental Science* 37: 012006.
Sharma, G. K., and V. V. Ghuge. 2025. "Development of a Framework for Assessment of Urban Growth Dynamics in Indian Metropolitan City: a Multi-Scale Analysis: Development of a Framework for Assessment of Urban Growth Dynamics in Indian Metropolitan City: a Multi-Scale Analysis." *Applied Spatial Analysis and Policy* 18 (3): 102.
Suetzl, BS, D. A. Strebel, A. Rubin, J. Wen, and J. Carmeliet. 2024. "Urban Morphology Clustering Analysis to Identify Heat-Prone Neighbourhoods in Cities." *Sustainable Cities and Society* 107: 105360.
Sun, G., X. Chen, X. Jia, et al. 2015. "Combinational Build-Up Index (CBI) for Effective Impervious Surface Mapping in Urban Areas." *IEEE Journal of Selected Topics in Applied Earth Observations and Remote Sensing* 9 (5): 2081–2092.
Team QD. 2024. We use the QGIS Geographic Information System (Version 3.40 "Bratislava"). [Software] Accessed on December 10, 2025 https://qgis.org.
Thomas, I., P. Frankhauser, B. Frenay, and M. Verleysen. 2010. "Clustering Patterns of Urban Built-Up Areas with Curves of Fractal Scaling Behaviour." *Environment and Planning B: Planning and Design* 37 (5): 942–954.

Toxqui, C., A. Padilla, A. Delgadillo, et al. 2025. "Deep Learning in Urban Studies through Multi-Spectral Satellite Imagery (Invited Paper)." *Proc of SPIE* 13710: 137100S.
UrbanAtlas. 2021. The ESA third party mission collection of the largest European urban areas recorded by the WorldView-2 satellite.
Valle, D., A. Wagemakers, A. Daza, and M.A.F. Sanjuan. 2022. "Characterization of Fractal Basins Using Deep Convolutional Neural Networks." *International Journal of Bifurcation and Chaos* 32 (13): 2250200.
Van Aelst, S., and P. Rousseeuw. 2009. "Minimum Volume Ellipsoid." *Wiley Interdisciplinary Reviews: Computational Statistics* 1 (1): 71–82.
Verma, P., and A. S. Raghubanshi. 2018. "Urban Sustainability Indicators: Challenges and Opportunities." *Ecological indicators* 93: 282–291.
Wang, J., and F. Biljecki. 2022. "Unsupervised Machine Learning in Urban Studies: a Systematic Review of Applications." *Cities* 129: 103925.
Waqar, M. M., J. F. Mirza, R. Mumtaz, and E. Hussain. 2012. "Development of New Indices for Extraction of Built-Up Area & Bare Soil from Landsat Data." *Scientific Reports* 1 (1): 4.
West, G. 2018. *Scale: The Universal Laws of Life, Growth, and Death in Organisms, Cities, and Companies*. Penguin.
Wu, X., X. Huang, and S. Guo. 2025. "The Fractal Characteristics and Risk Indicators of Urban Ecological Environment Vulnerability Evolution." *Ecological Informatics* 86: 103033.
Yu, T., B. S. Sützl, and M. van Reeuwijk. 2023. "Urban Neighbourhood Classification and Multi-Scale Heterogeneity Analysis of Greater London." *Environment and Planning B: Urban Analytics and City Science* 50 (6): 1534–1558.

## Appendices

### *Appendix A. Further WV-2 satellite images and MBEI maps, built-up indices and fractal dimensions*

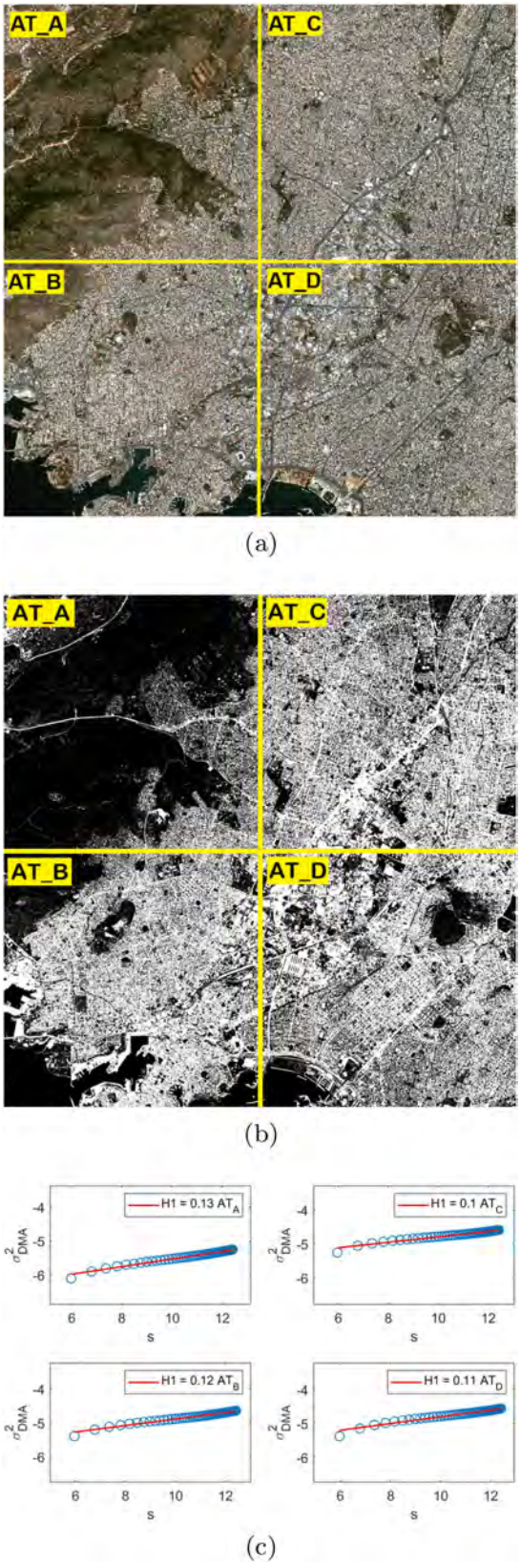


**Figure A1.** (a) WorldView-2 high resolution satellite image N37-951 (Athens). (b) *MBEI* map with built-up density values for the four sectors $\mathcal{B}_A = 0.16$, $\mathcal{B}_B = 0.53$, $\mathcal{B}_C = 0.64$, and $\mathcal{B}_D = 0.59$. (c) Log–log plots of $\sigma^2_{DMA}$ for each red band sub-image of (a).

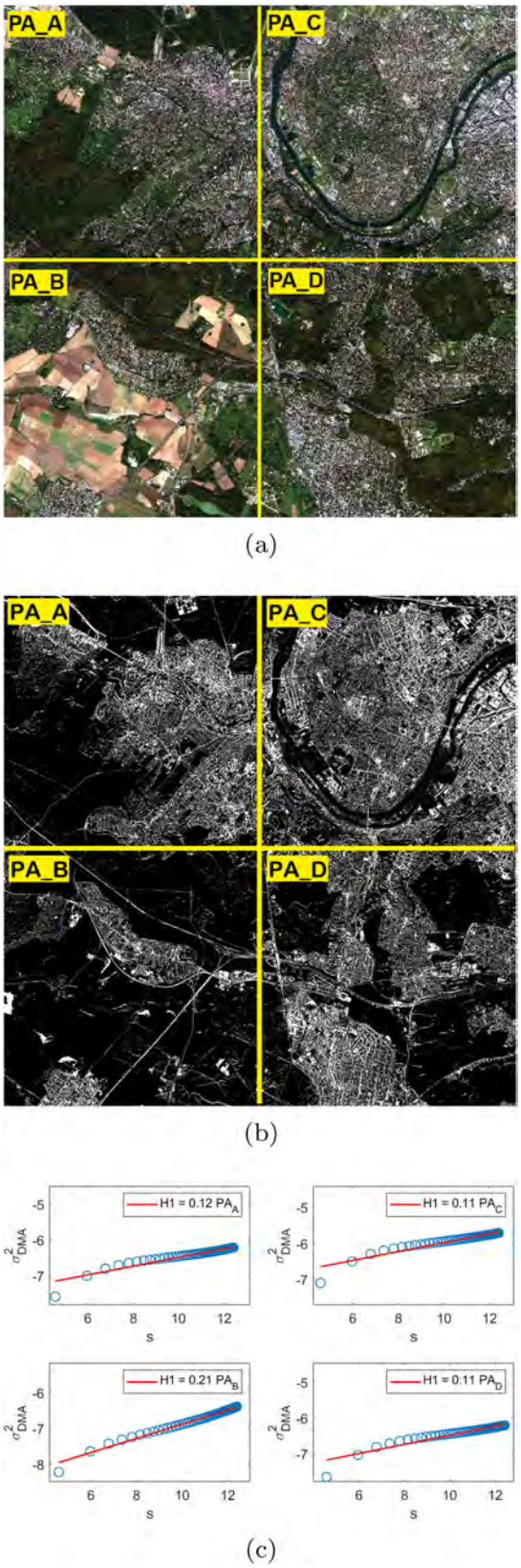


**Figure A2.** (a) WorldView-2 high resolution satellite image N48-845 (Paris). (b) *MBEI* map (Paris) with built-up density values for the four sectors $\mathcal{B}_A = 0.19$, $\mathcal{B}_B = 0.09$, $\mathcal{B}_C = 0.32$, and $\mathcal{B}_D = 0.21$. (c) Log–log plots of $\sigma^2_{DMA}$ for each red-band sub-image of (a).

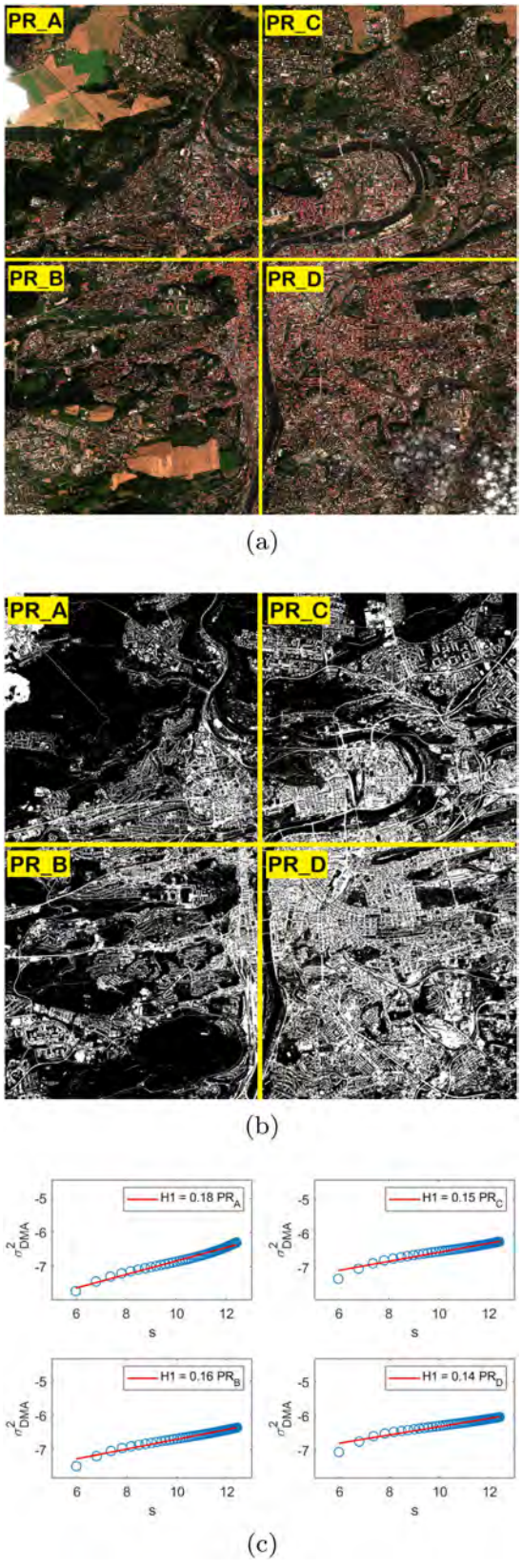


**Figure A3.** (a) WorldView-2 high resolution satellite image N50-090 (Prague). (b) *MBEI* map with built-up density values for the four sectors $\mathcal{B}_A = 0.22$, $\mathcal{B}_B = 0.27$, $\mathcal{B}_C = 0.33$, and $\mathcal{B}_D = 0.48$. (c) Log–log plots of $\sigma^2_{DMA}$ for each red-band sub-image of (a).

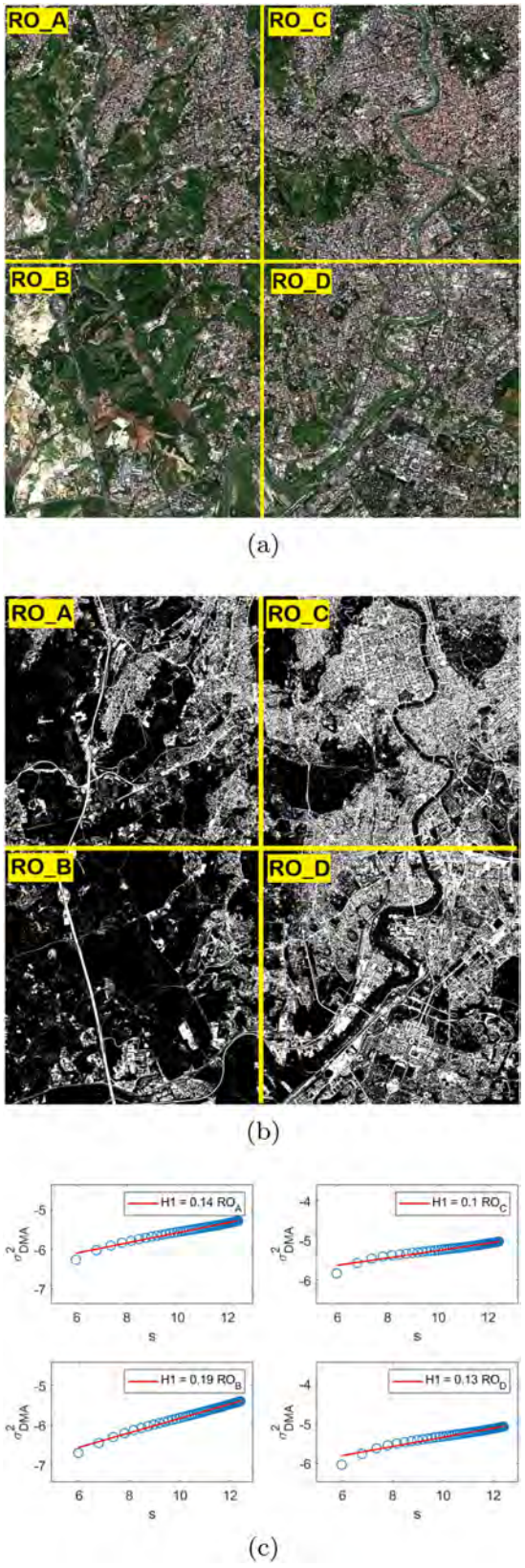


**Figure A4.** (a) WorldView-2 high resolution satellite image N41-863 (Rome). (b) *MBEI* map with built-up density values of the four sectors $\mathcal{B}_A = 0.26$, $\mathcal{B}_B = 0.15$, $\mathcal{B}_C = 0.44$, and $\mathcal{B}_D = 0.40$. (c) Log–log plots of $\sigma^2_{DMA}$ for each red band sub-image of (a).

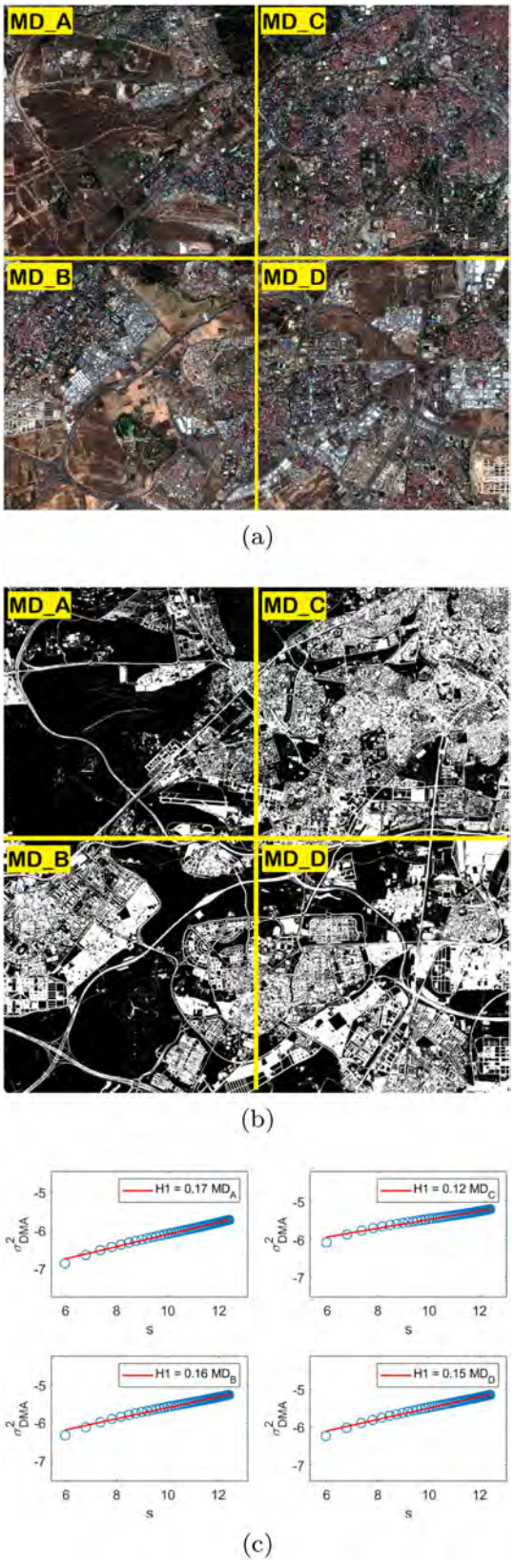


**Figure A5.** (a) WorldView-2 satellite high resolution image N40-331 (Madrid). (b) *MBEI* map with density values of the four sectors $\mathcal{B}_A = 0.18$, $\mathcal{B}_B = 0.36$, $\mathcal{B}_C = 0.50$, and $\mathcal{B}_D = 0.48$. (c) Log–log plots of $\sigma^2_{DMA}$ for each red band sub-image of (a).

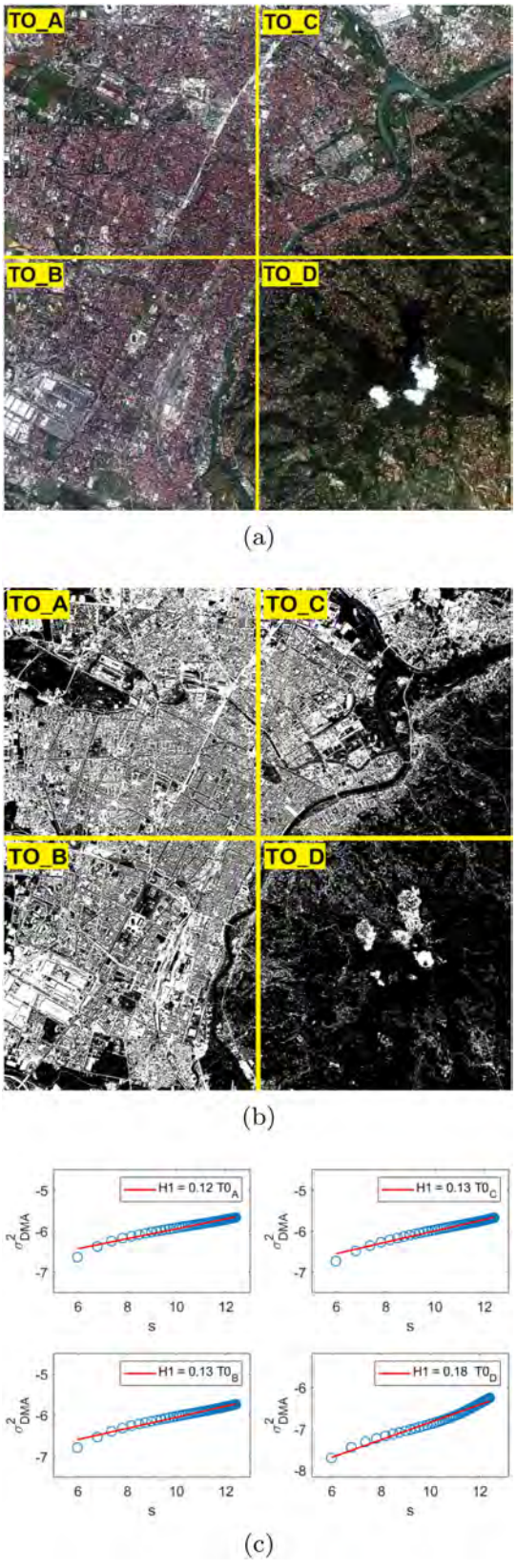


**Figure A6.** (a) WorldView-2 satellite high resolution image N45-024 (Torino). (b) *MBEI* map with built-up density values of the four sectors $\mathcal{B}_A = 0.56$, $\mathcal{B}_B = 0.54$, $\mathcal{B}_C = 0.38$, and $\mathcal{B}_D = 0.11$. (c) Log–log plots of $\sigma^2_{DMA}$ for each red-band sub-image of (a).

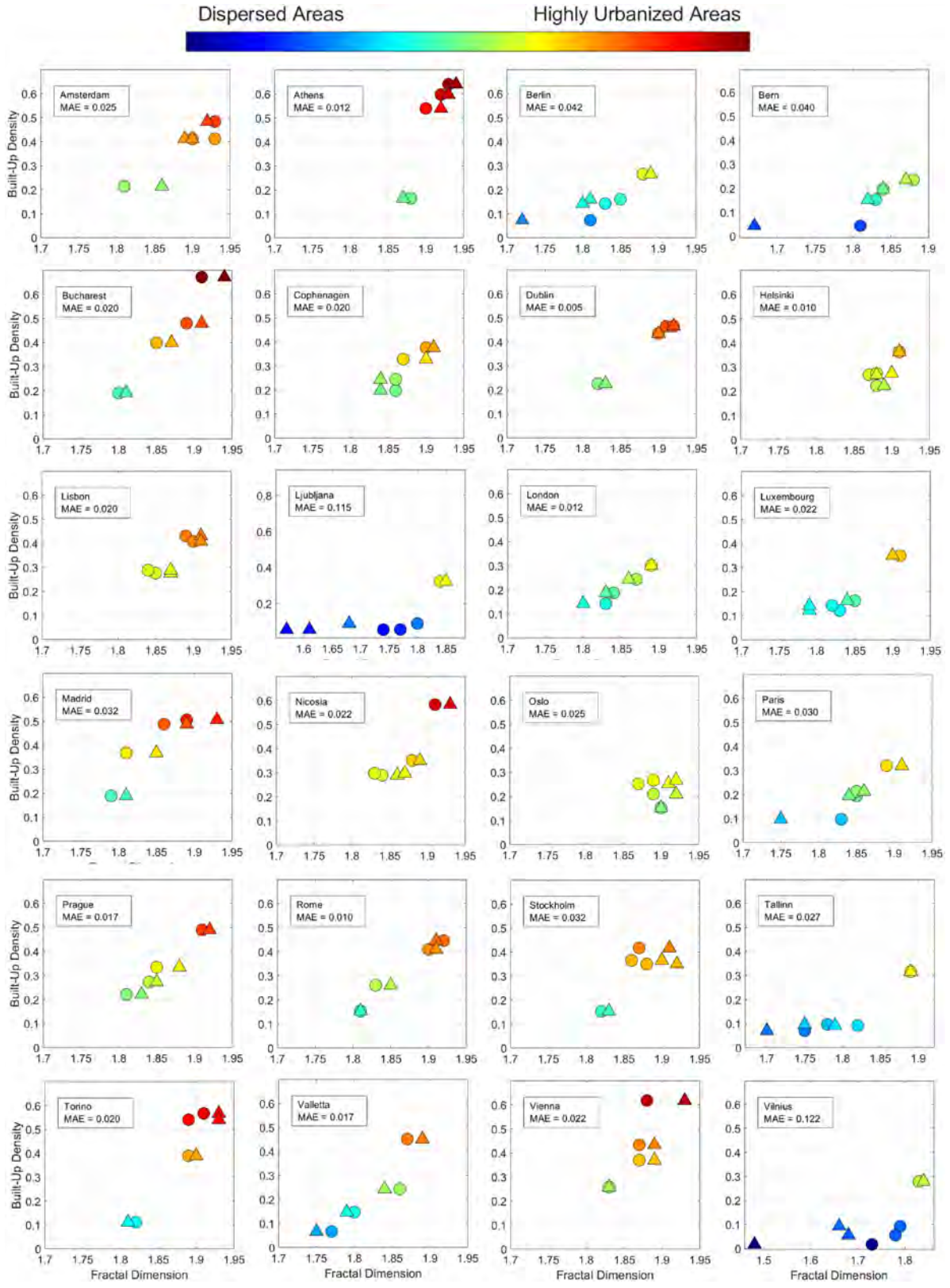


**Figure A7.** Relative positioning of the $D_f$ values corresponding to each area within the city remains consistent across methods, reflecting the influence of the specific algorithm used. In this comparison: DMA is represented by the symbol '○', and BC by the symbol 'Δ'. Mean Absolute Error (MAE) between paired observations in DMA and Box Counting.

## Appendix B. Threshold range optimization for built-up extraction

To improve the built-up extraction algorithm and ensure the robustness of the proposed method across different urban environments, the threshold ranges for the built-up mask ($\overline{M}$) and the preliminary binarized *NBEI* map ($B_0$) were rigorously optimized to identify the optimal set of parameters $\theta = \{R, T, U\}$ that maximize the discrimination between built-up structures and bare soil areas in the *MBEI* map. To achieve this, a Mosaic Strategy was implemented to create a representative training dataset that captures the spectral variability of these classes across all the cities. Two reference mosaics were constructed by aggregating $K = 49$ cropped patches from diverse scenes within the WorldView-2 high-resolution dataset (Figure B1):

- **Built-up Mosaic ($M_{built}$)**: Composed exclusively of urban structures (residential, industrial, dense/dispersed) from multiple cities.
- **Bare Soil Mosaic ($M_{soil}$)**: Composed of bare ground, plowed fields, exposed earth regions, and clouds.

The optimization problem is formulated to maximize a fitness function $J(\theta)$, defined as the difference between the correctly classified built-up pixels in the positive mosaic and the misclassified soil pixels in the negative mosaic:

$$\theta_{opt} = \arg\max_{R,T,U} J(R, T, U), \tag{B1}$$

$$J(R, T, U) = \sum_{(x,y)\in M_{built}} \mathbb{I}[MBEI(x, y; \theta) = 1] - \sum_{(x,y)\in M_{soil}} \mathbb{I}[MBEI(x, y; \theta) = 1], \tag{B2}$$

where $\mathbb{I}[\cdot]$ is the indicator function equal to 1 if the condition is met (pixel classified as built-up) and 0 otherwise. The parameter search space $\Omega$ was defined based on the cumulative histogram of the *NBEI* and *WVBI* indices:

- NBEI Soil Exclusion Range ($R$): [0.00, 0.20] with step $\Delta R = 0.0005$.
- WVSI Soil Detection Range ($T$): [0.15, 0.50] with step $\Delta T = 0.005$.
- NBEI Built-up Acceptance Range ($U$): [−0.20, 0.20] with step $\Delta U = 0.005$.

A grid search algorithm evaluated every combination within $\Omega$. The optimization yielded the following global Optimal Intervals for this dataset:

- $\overline{M}$ (NBEI) exclusion: $R \in [0.0395, 0.149]$
- $\overline{M}$ (WVSI) detection: $T \in [0.048, 0.245]$
- $B_0$ threshold: $U \in [-0.130, 0.149]$

The above values have been globally applied to the entire image dataset.

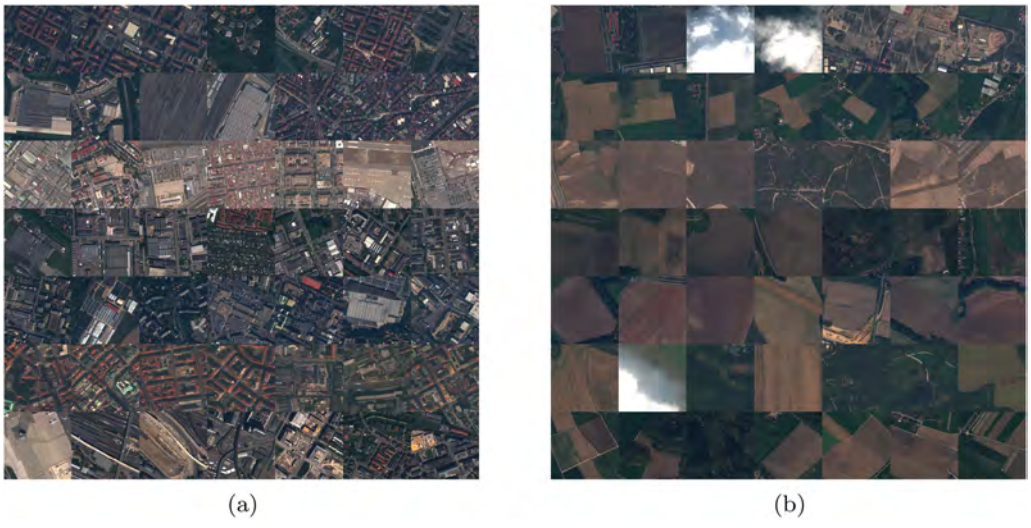


**Figure B1.** Training dataset for threshold optimization constructed to ensure generalization: (a) Built-up mosaic ($M_{built}$), (b) Bare soil mosaic ($M_{soil}$), of size 1400 × 1400 each.

### B.1. Quantitative validation and accuracy assessment

To rigorously evaluate the performance of the proposed method, a pixel-by-pixel comparative analysis was conducted between the algorithm outputs and manually labeled Ground Truth (GT) masks using QGIS (Team QD 2024). Unlike sparse point sampling, this approach quantifies the spatial coherence of the built-up extraction across the entire extent of representative test tiles. The validation process assesses three distinct stages of the proposed pipeline to demonstrate the step-wise improvement of the methodology:

- **NBEI (Raw):** initial thresholding of the Normalized Built-up Extraction Index without soil removal.
- **MBEI (Masked):** upon applying the bare soil mask ($\overline{M}$) and before the morphological operation.
- **MBEI (+Morph.):** after applying the morphological closing to restore structural integrity.

For each stage, a confusion matrix was computed by comparing the binary prediction map ($P$) against the ground truth ($GT$). The pixels were categorized as True Positives ($TP$), True Negatives ($TN$), False Positives ($FP$, indicating overestimation or noise), and False Negatives ($FN$, indicating the omission of buildings). The classification performance was evaluated using standard metrics derived from the confusion matrix: Overall Accuracy (OA), F1-Score, and Intersection over Union (IoU) (Maxwell, Warner, and Guillén 2021).

Table B1 summarizes the quantitative results. The raw NBEI exhibits a high rate of False Positives due to spectral confusion with bare soil. The application of the soil mask (MBEI Masked) significantly improves Precision and IoU by eliminating these artifacts. Finally, the morphological closing (MBEI Final) recovers the spatial continuity of the buildings, balancing the omission errors (FN) and yielding the highest F1-Score and IoU.

To visualize the spatial distribution of errors, RGB difference maps were generated (Figure B2). In these maps, **Green** pixels represent correct detections (TP), **Red** pixels indicate overestimation (FP, e.g. soil misclassified as urban), and **Blue** pixels denote omission errors (FN). As observed in Figures B2e and B2f, the proposed MBEI successfully suppresses the red noise characteristic of the raw NBEI (Figures B2a and B2b) while maintaining the structural definition of the urban footprint.

To demonstrate the transferability of the optimized thresholding across diverse urban morphologies, a qualitative comparison was conducted on four representative European cities: Madrid, Paris, Prague, and Zurich. Figure B3 displays the visual assessment of the built-up extraction performance. Column (a) presents the reference RGB composites. Column (b) shows the segmentation results using the standard NBEI with global thresholds, where significant overestimation is observed, particularly in peripheral zones with bare soil. In contrast, column (c) illustrates the results obtained with the proposed MBEI using the optimized parameters derived in this appendix. As highlighted by the red squares, the MBEI successfully filters out the bare soil artifacts while preserving the dense urban fabric, confirming that the optimization strategy is robust against the spectral variability found in different metropolitan environments.

Finally, to demonstrate the transferability to other satellite sensors, the optimized threshold ranges obtained from the WV-2 dataset were directly applied to WV-3 imagery. As shown in Figure B4, the same optimized threshold ranges produce consistent built-up extraction results. The comparison was performed using the Vienna sub-sectors A and B (N48-181) from the Urban Atlas WV-2 dataset, and the same RoI of Vienna (N48-199) from WV-3 with similar multispectral bands. These results suggest that the optimized thresholds exhibit good transferability across sensors; nevertheless, for imagery acquired by other sensors or regions, re-optimization may be required to achieve the best segmentation performance.

**Table B1.** Quantitative comparison of built-up extraction performance across different processing stages. The metrics are expressed in percentage (%).

| Method/Stage | Precision | Recall | F1-Score | IoU | OA |
|---|---|---|---|---|---|
| NBEI (Raw) | 59.03 | 76.52 | 66.65 | 49.98 | 67.56 |
| MBEI (Masked) | 83.23 | 62.33 | 71.28 | 55.37 | 78.72 |
| **MBEI (+Morph.)** | **83.14** | **76.35** | **79.60** | **66.11** | **83.42** |

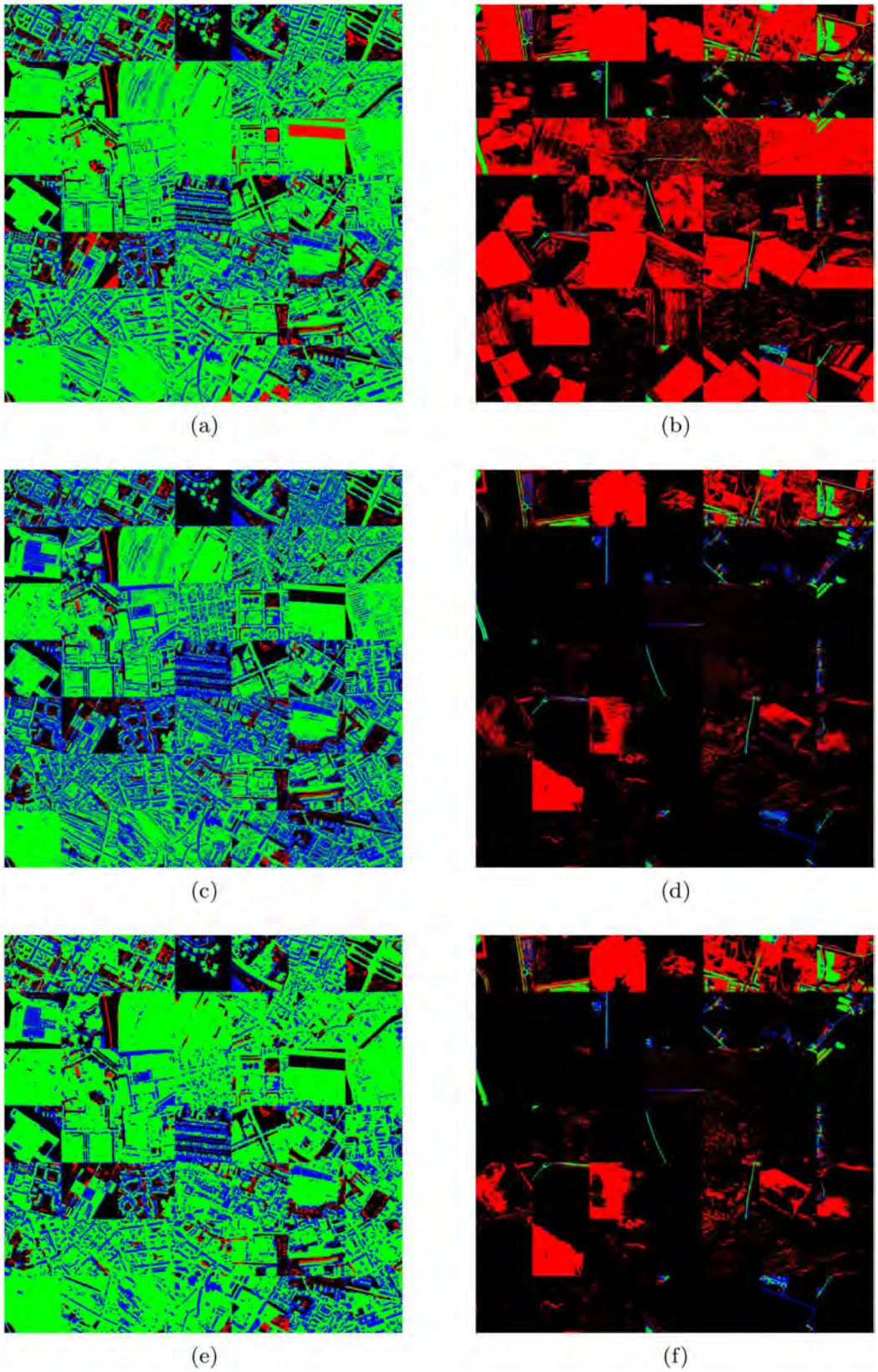


**Figure B2.** Visual validation of the built-up extraction. (a) and (b) Error maps of the raw NBEI, showing significant overestimation (Red areas). (c) and (d) Error maps of the MBEI without morphological closing, showing significant eroded urban structures (Blue areas). (e) and (f) Error map of the proposed MBEI, showing high agreement (Green areas) and reduced noise. Color code: Green = Correct (TP), Red = False Positive, Blue = False Negative.

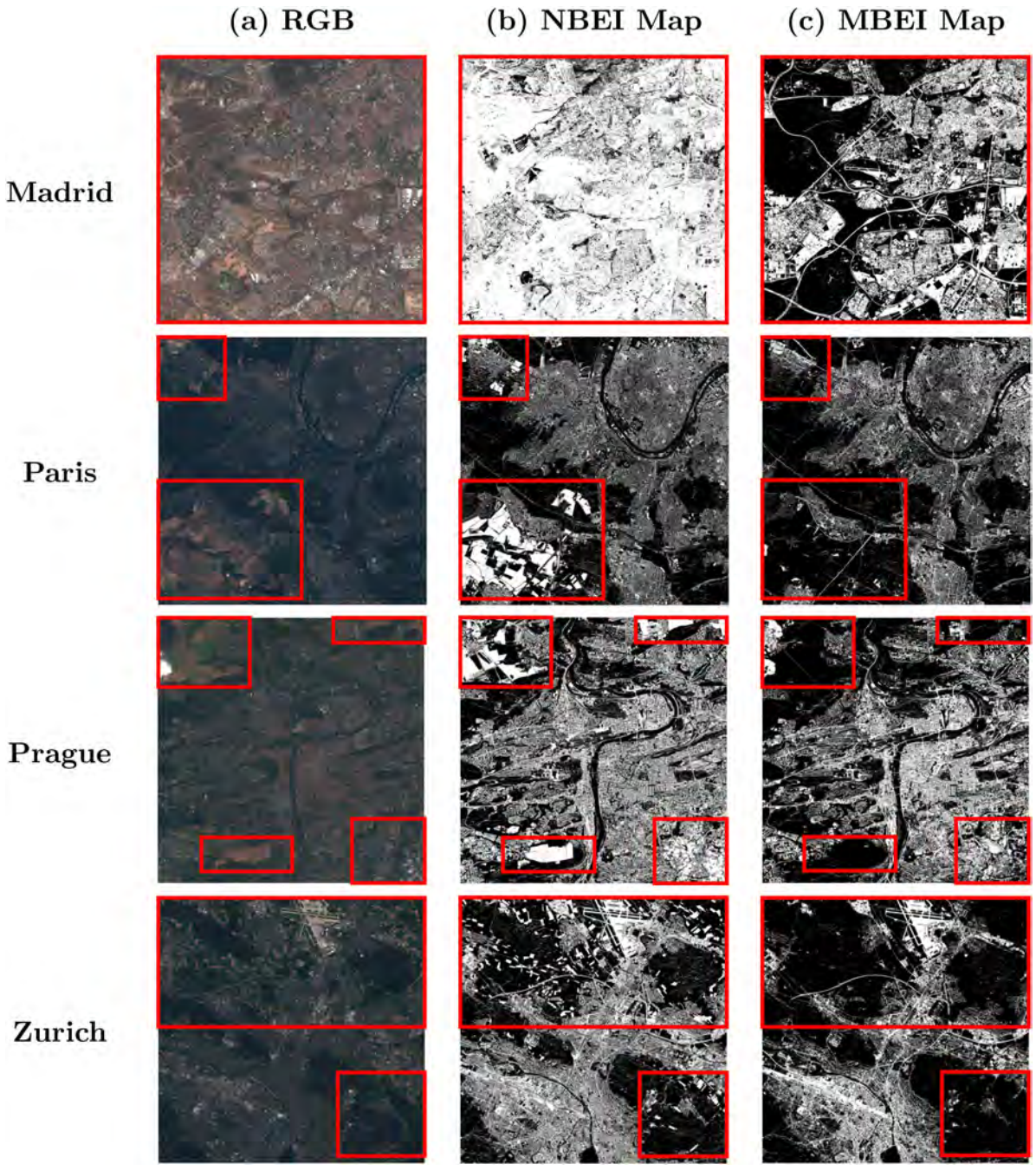


**Figure B3.** Built-up extraction maps. (a) Reference *RGB* images. Comparative results of image segmentation using (b) *NBEI* with a built-up threshold, (c) the proposed *MBEI* approach with the optimized threshold. Red squares highlight the bare soil areas successfully removed in the *MBEI* map.

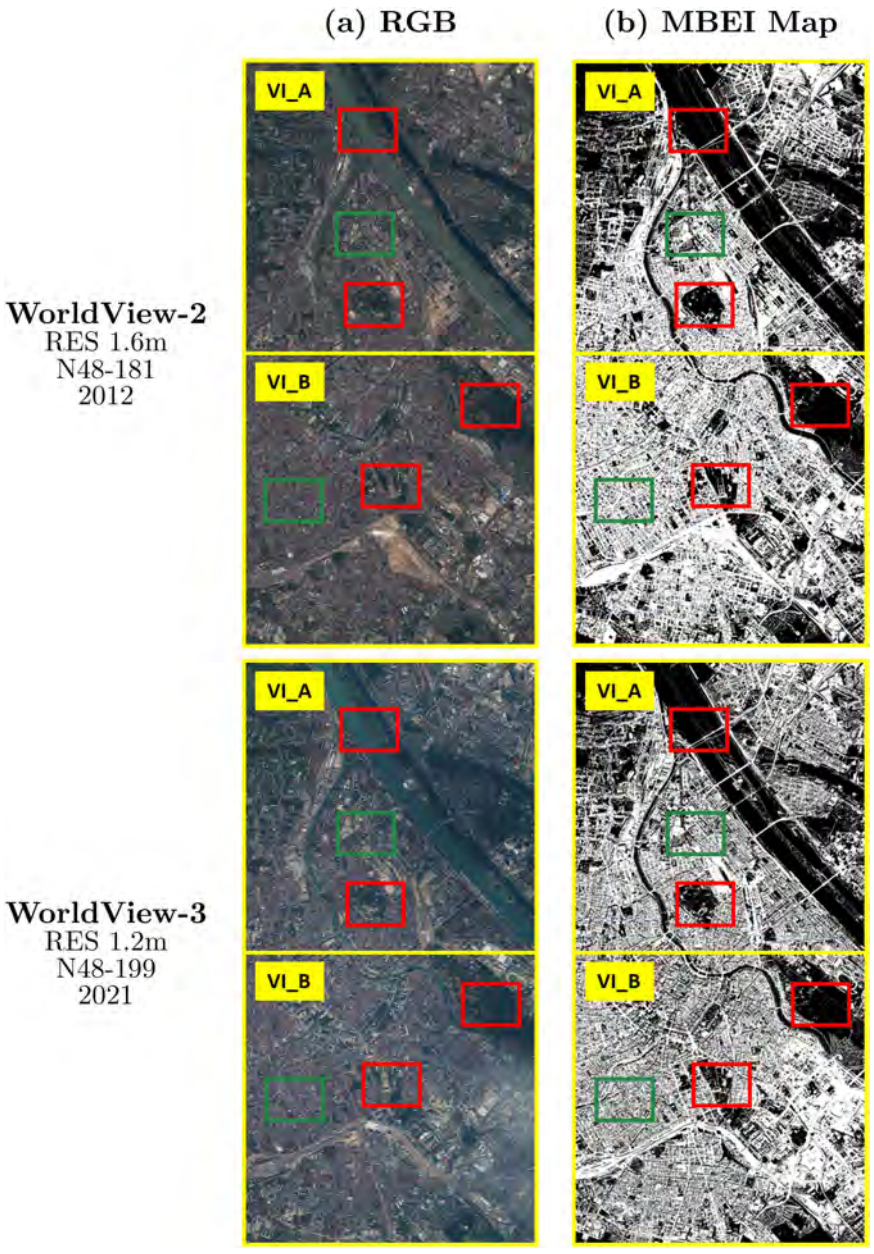


**Figure B4.** Transferability assessment of the proposed approach to a different satellite sensor without re-optimizing the threshold ranges. Column (a) shows the RGB Vienna images, whereas column (b) presents the corresponding *MBEI* maps obtained using the globally optimized thresholds. Green boxes indicate representative built-up structures correctly identified by the proposed method, whereas red boxes highlight non-built-up elements successfully rejected from the urban mask.

## *Appendix C. Transferability of the method to current data*

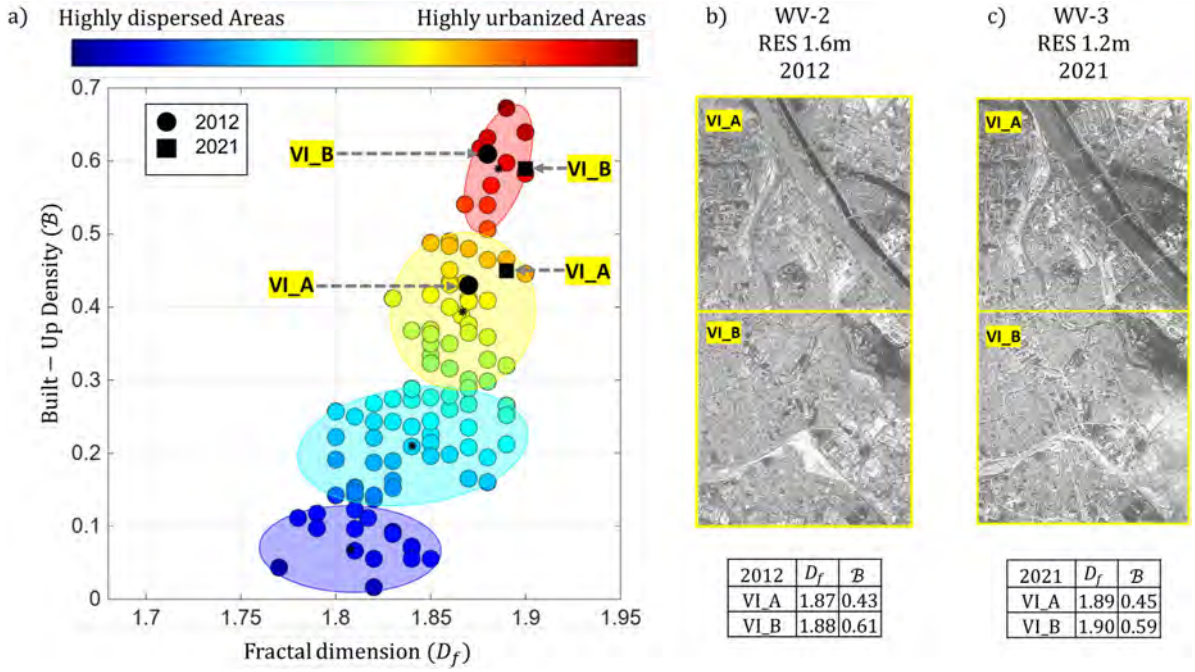


| 2012 | $D_f$ | $\mathcal{B}$ |
|---|---|---|
| VI_A | 1.87 | 0.43 |
| VI_B | 1.88 | 0.61 |

| 2021 | $D_f$ | $\mathcal{B}$ |
|---|---|---|
| VI_A | 1.89 | 0.45 |
| VI_B | 1.90 | 0.59 |

**Figure C1.** a) Built-up density and fractal dimension clustered by means of the *MVEE* ($m_W$) algorithm by implementing the *MBEI*/*DMA* method on the same *RoI* of Vienna images: b) WV-2 N48-181 and c) WV-3 N48-199, respectively dated 2012 and 2021. The urban features belong to the same clusters, witnessing approach robustness and selectivity. However, the fractal dimensions and the built-up density are practically unchanged. The constant values of the fractal dimension ($D_f = 2 - H$) can be understood consistently with the property of the Hurst exponent $H$ of being scale independent for self-similar fractal surfaces.

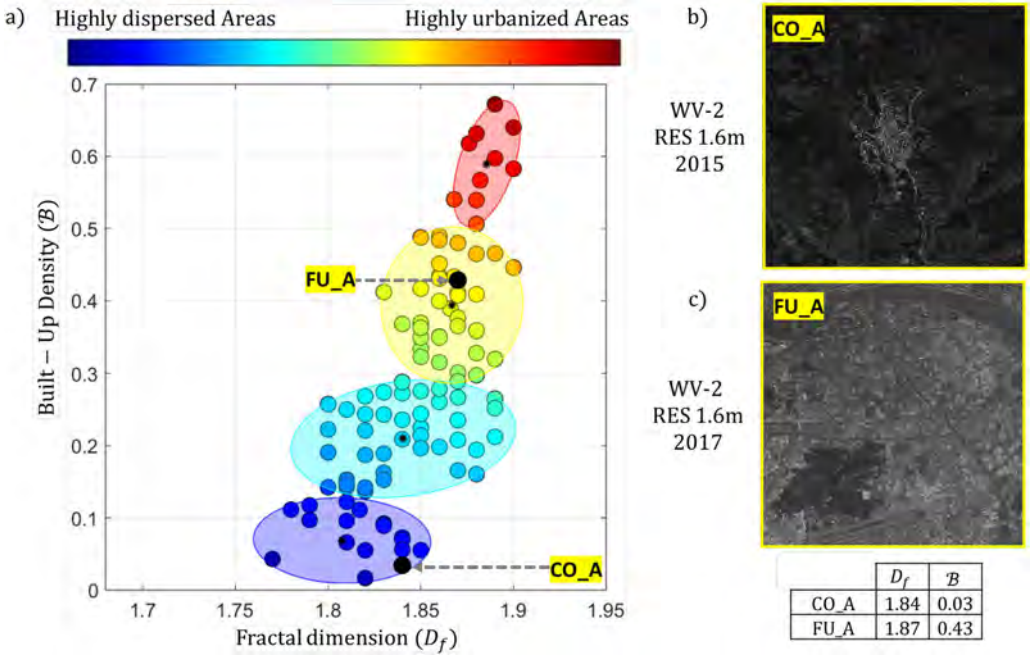


| | $D_f$ | $\mathcal{B}$ |
|---|---|---|
| CO_A | 1.84 | 0.03 |
| FU_A | 1.87 | 0.43 |

**Figure C2.** a) Built-up density and fractal dimension clustered by means of the *MVEE* ($m_W$) algorithm for the images b) WV-2 N17-094 (Copainala, Mexico, 2015) and c) WV-2 N26-033 (Fuzhou, China, 2017). The urban feature values are estimated by implementing the *DMA* method on high-resolution (red band) images to validate the transferability of the MBEI method without re-tuning. As shown, the urban features fit to the predefined clusters.

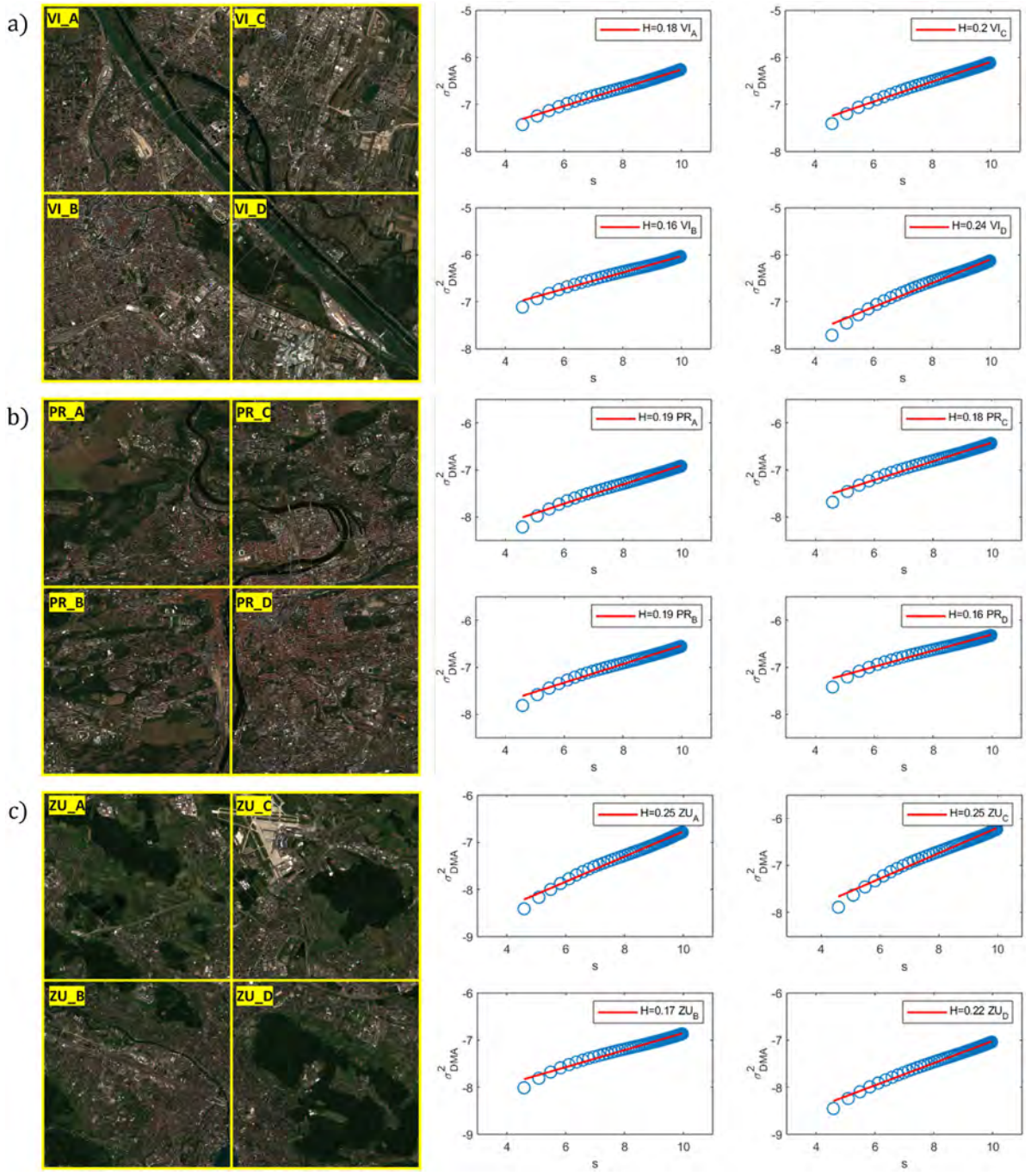


**Figure C3.** Sentinel-2LA satellite images (left panels) recorded in 2025 for the cities: a) Vienna, b) Prague, and c) Zurich. The right panels show the log-log plots of $\sigma^2_{DMA}$ for each red-band sector. The Hurst exponent values are estimated from the same RoI as defined in Carbone, Murialdo, and Pieroni (2022).

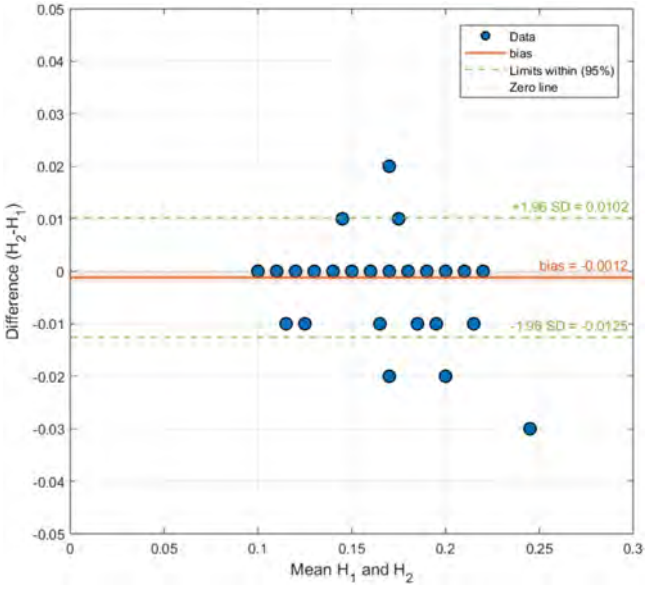


**Figure C4.** Bland-Altman analysis comparing the Hurst exponent estimated by the DMA method. Values derived from a total of 112 sectors distributed across European cities from WV-2 imagery at high and low resolution. The plot shows the difference between the method against their average, with the bias, 95% limits of agreement, and the zero line.